




Cite this: *EES Catal.*, 2023,  
1, 230

## Recent advances in perovskite oxide electrocatalysts for Li–O<sub>2</sub> batteries

Lulu Lyu,<sup>†a</sup> Seonyong Cho<sup>†a</sup> and Yong-Mook Kang  <sup>\*,abc</sup>

Lithium–oxygen batteries (LOBs) have been anticipated as promising energy-storage devices; however, their practical application is plagued by low energy efficiency, small capacity, and the short cycle life. When applied as air cathodes for LOBs, perovskite oxides exhibit an enormous potential for favorable battery performance due to their catalytic activity for the oxygen reduction reaction (ORR) and oxygen evolution reaction (OER). Their tunable compositions, diverse structures and unique electronic properties allow flexible manipulation of their catalytic activity. This mini-review comprehensively describes recent advances in perovskite oxide electrocatalysts for LOBs. First, the energy-storage mechanism of LOBs and crucial catalytic descriptors of perovskites for the ORR/OER are analyzed. Then, several ingenious tactics to promote the catalytic activity of perovskite oxides are highlighted. A discussion of synthetic protocols for the preparation of perovskite oxides follows, including how the nanostructure, morphology and composition of perovskite oxides can be controlled by different methods and the effect of these on catalytic performance. Additionally, A-/B-/O-site regulation, oxygen vacancies, and the composites of perovskites and functional materials are thoroughly investigated. Finally, we summarize the challenges and outlook of perovskite oxide electrocatalysts for LOBs.

Received 7th February 2023,  
Accepted 16th March 2023

DOI: 10.1039/d3ey00028a

[rsc.li/eescatalysis](http://rsc.li/eescatalysis)

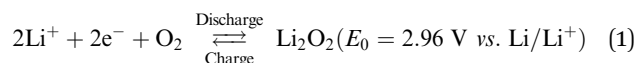
### Broader context

The transition from fossil fuels to renewable energy is a pivotal approach to realizing a low-carbon economy, which stimulates the exploration of electrochemical energy storage devices. Lithium–oxygen batteries (LOBs) have been regarded as promising energy-storage systems, while their inferior energy efficiency, low capacity, and poor cycle life greatly hinder their practical applications. Owing to their catalytic activity for the oxygen reduction reaction (ORR) and oxygen evolution reaction (OER), perovskite oxides with a formula of ABO<sub>3</sub> have been investigated as air cathodes for LOBs. Their catalytic activity can be flexibly adjusted by different cation/anion species, distinct nanostructures and unique electronic properties. This mini-review aims to comprehensively provide recent advances in perovskite oxide electrocatalysts for LOBs. It begins with introducing the fundamental energy-storage mechanism of LOBs, and catalytic descriptors of perovskites for the ORR/OER. Next, strategies to improve the catalytic activity of perovskite oxides are highlighted, including the size effect, nanostructure engineering, A-/B-/O-site regulation, oxygen vacancies, and composites of perovskites with other functional materials. Finally, the challenges and outlook of perovskite oxide electrocatalysts for LOBs are given.

## 1. Introduction

World energy consumption is expected to be 50% higher than 2018 levels (576 EJ) by 2050 (864 EJ). To achieve net zero fossil fuel use by 2050, the annual growth rate of renewable energy production must expand by a factor of 6–8.<sup>1</sup> The soaring demand for electrical energy storage and conversion systems has driven

exploration into metal-ion batteries, metal-air batteries, and redox-flow batteries.<sup>2–6</sup> Lithium-air batteries have a superior theoretical energy density of above 5000 W h kg<sup>−1</sup> (Fig. 1), and a large theoretical open circuit voltage of 2.96 V (eqn (1)).<sup>6–8</sup> Electric vehicles using these batteries may have a driving range of more than 550 kilometers.<sup>9</sup> As shown in Fig. 2(a), lithium–oxygen batteries (LOBs) are composed of a metallic lithium anode, an air cathode and a Li<sup>+</sup>-containing aprotic electrolyte.<sup>10–14</sup> The oxygen reduction reaction (ORR) and oxygen evolution reaction (OER) occurring at the cathode dominate the discharging and charging processes of LOBs, respectively.<sup>15–19</sup>



<sup>a</sup> Department of Materials Science and Engineering, Korea University, Seoul 02841, Republic of Korea. E-mail: [dake1234@korea.ac.kr](mailto:dake1234@korea.ac.kr)

<sup>b</sup> KU-KIST Graduate School of Converging Science and Technology, Korea University, Seoul, 02841, Republic of Korea

<sup>c</sup> Energy Storage Research Center, Clean Energy Research Division, Korea Institute of Science and Technology (KIST), Seoul 02792, Republic of Korea

<sup>†</sup> These authors contributed equally to this work.



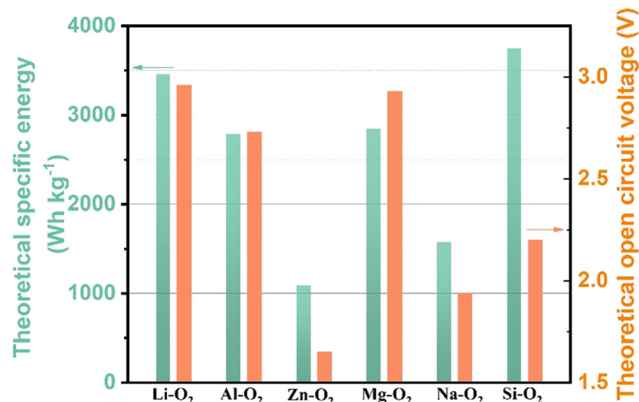


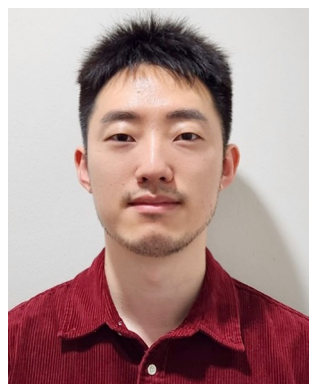
**Fig. 1** The theoretical specific energy and open circuit voltage of various metal–air batteries. The specific energy is calculated by multiplying the theoretical specific capacity by the voltage.

Though LOBs hold great promise due to their high theoretical energy density, several crucial issues should be overcome to realize their real-world application. Specifically, the insulating discharged product of Li<sub>2</sub>O<sub>2</sub> covered on the cathode surface blocks the diffusion pathway for oxygen and electrolyte ions,



**Lulu Lyu**

*Lulu Lyu received her PhD (2021) from the Department of Convergence Science and Technology at Seoul National University. She is currently a research professor in Department of Materials Science and Engineering at Korea University. Her research focuses on nanomaterials and their applications for electrocatalysts and energy-storage materials.*



**Seonyong Cho**

*Seonyong Cho is a PhD student in the department of materials science and engineering at Korea University under the supervision of Prof. Yong-Mook Kang. His research area is catalysts and system design for lithium–air batteries.*



**Yong-Mook Kang**

*Yong-Mook Kang completed his BS (1999), MS (2001), and PhD (2004) at Korea Advanced Institute of Science and Technology. He has been a senior researcher at Samsung SDI Co., Ltd. He is currently a professor at Department of Materials Science and Engineering in Korea University, Republic of Korea. His research area covers electrode or catalyst materials for rechargeable batteries. He has been appointed as RSC (Royal Society of Chemistry)*

*fellow and representative of Korea from 2015 and a member of Y-KAST (Young Korean Academy of Science and Technology) from 2020.*



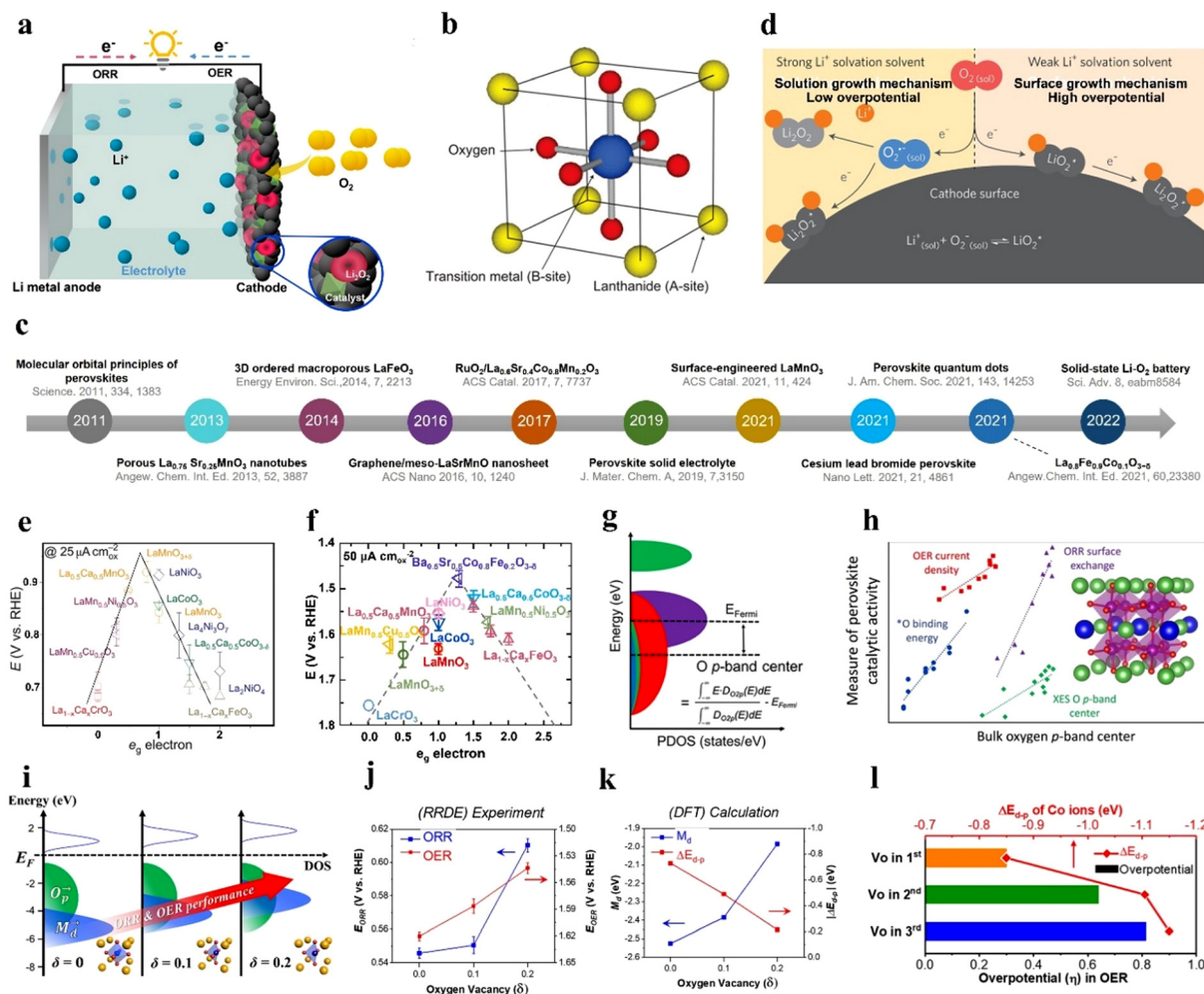


**Fig. 2** Overview and mechanisms of LOBs, and descriptors for the catalytic activity of perovskite oxides. (a) Illustration of LOBs. (b)  $ABO_3$  perovskite structure. (c) Timeline of research findings of perovskite oxides for LOBs. (d) Solution growth and surface-growth mechanisms in the LOB. Reproduced with permission.<sup>49</sup> Copyright 2016, Springer Nature. (e) Potentials as a function of  $e_g$  orbitals in perovskites. (b) and (e) Reproduced with permission.<sup>33</sup> Copyright 2011, Springer Nature. (f) OER performance as a function of the  $e_g$  orbital in perovskites. (g) Projected density of states (PDOS) of the O 2p orbit. (h) Catalytic activity as a function of the oxygen p-band center. (g) and (h) Reproduced with permission.<sup>50</sup> Copyright 2019, American Chemical Society. (i) The relationship between the electronic structure of  $Sm_{0.5}Sr_{0.5}CoO_{3-\delta}$  and ORR/OER performance. (j) The relationship between ORR/OER activity and  $V_o$  based on experimental results. (k) The relationship between  $\Delta E_{d-p}$ ,  $M_d$ , and  $V_o$  based on DFT results. (l) Overpotential and  $\Delta E_{d-p}$  values of the OER according to the  $V_o$  position in the 1st, 2nd, and 3rd layer of perovskites. (i)–(l) Reproduced with permission.<sup>51</sup> Copyright 2020, American Chemical Society.

when applied in non-aqueous LOBs, generally exhibit low Brunauer–Emmett–Teller (BET) surface areas, few morphologies and large particle sizes, which compromises their catalytic activity and the performance of LOBs.

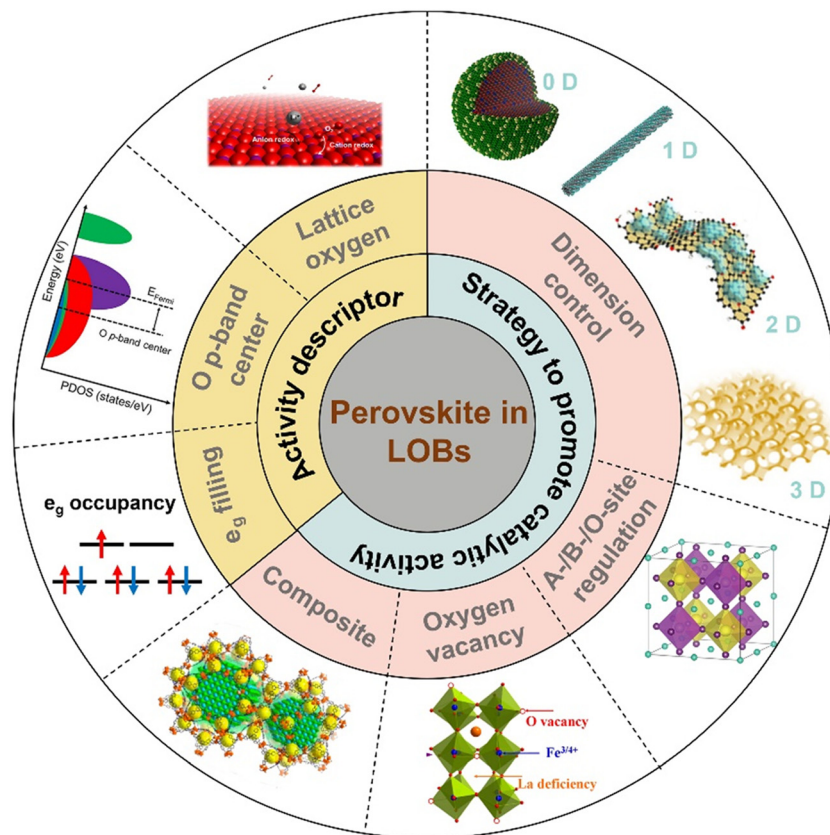
The catalytic activity of perovskites can be flexibly tuned by several strategies. First, nanosizing bulk perovskites can expose enriched active sites and facilitate the diffusion of reactive species.<sup>40,41</sup> Second, substituting A-, B- and O-sites with foreign elements can change the electronic and crystal structures of the perovskites, thereby tuning the binding strength with oxygen intermediates.<sup>42–44</sup> Third, oxygen vacancies ( $V_o$ ) can change the valence state of B-site cations and thus modulate the interaction between the metal ion and oxygen molecules.<sup>45</sup> Lastly, heterostructures combining perovskites with carbon materials, metal–organic frameworks (MOFs), and MXenes possess large

surface areas, porous structures, and enhanced charge transfer efficiencies, which accommodate more LOB discharge products and increase the utilization of active sites.

The anticipated high energy efficiency, superior capacity, and long cycle life of LOBs are highly governed by the physico-chemical properties of perovskite-based air cathodes. Even though review papers related to perovskite-based catalysts in aqueous solutions have been reported,<sup>46–48</sup> reviews that thoroughly outline recent advances in aprotic solutions for LOBs are rare. Hence, this review provides a timely and comprehensive understanding of recent advances towards perovskite catalysts for LOBs. Scheme 1 shows an overview of the perovskite-based electrocatalysts for LOBs in this review. Fig. 2(c) illustrates the timeline of the most impactful research findings related to perovskite oxides used for LOBs. Initially in







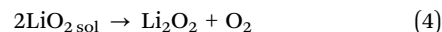
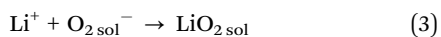
Scheme 1 Schematic illustration of perovskite oxides as cathodes for LOBs.

this mini-review, the energy-storage mechanisms of LOBs and the activity descriptors of perovskite oxides for the ORR/OER are demonstrated. Next, key strategies to boost the catalytic activity of perovskite oxides are described, including morphology and nanostructure control, A-/B-/O-site regulation, oxygen vacancies, and composites with other functional materials. Finally, a summary of the challenges and outlook of perovskite oxide electrocatalysts for LOBs is provided.

## 2. Mechanisms of LOBs

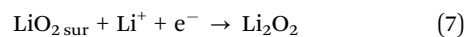
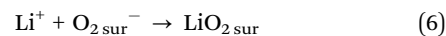
The growth and distribution of  $\text{Li}_2\text{O}_2$  influences the reaction overpotential of an LOB. The electronic structures and morphologies of  $\text{Li}_2\text{O}_2$  depend on solution growth (eqn (2)–(4)) or surface-growth mechanisms (eqn (5)–(7)), as shown in Fig. 2(d).<sup>52</sup> The two growth mechanisms are associated with the solubility of the  $\text{LiO}_2$  intermediate. It has been reported that the donor number of the solvent can influence the solubility of  $\text{LiO}_2$  and thus manipulates  $\text{O}_2$  reduction pathways.<sup>53</sup>

**Solution growth mechanism:**  $\text{O}_2$  molecules are reduced to superoxide ( $\text{O}_2^-$ ), which dissolves into the electrolyte (expressed as  $\text{O}_{2\text{sol}}^-$ ).  $\text{Li}^+$  ions react with  $\text{O}_{2\text{sol}}^-$  to generate soluble  $\text{LiO}_{2\text{sol}}$ . The  $\text{LiO}_{2\text{sol}}$  intermediate in the electrolyte becomes  $\text{Li}_2\text{O}_2$  after a disproportionation reaction.



The solution-growth mechanism can be promoted by enhancing  $\text{LiO}_2$  solubility in a high-donor-number-based electrolyte, generating toroidal  $\text{Li}_2\text{O}_2$  made of lamellae and leading to a high discharge capacity. Due to the loose contact between  $\text{Li}_2\text{O}_2$  and the catalyst and the low conductivity of the  $\text{Li}_2\text{O}_2$  toroid, an LOB based on the solution-growth model exhibits a low round-trip efficiency and high charge overpotential despite its high specific capacity.<sup>52,54</sup> Moreover, a solvent with high polarity is easily affected by nucleophilic attack by  $\text{O}_2^-$ .<sup>55</sup> Efforts have been made to realize surface growth mechanisms by adding 2,5-di-*tert*-butyl-1,4-benzoquinone (DBBQ) in a low-donor-number solvent (LiTFSI in ether), where DBBQ avoided the direct formation of  $\text{Li}_2\text{O}_2$  on the cathode surface.<sup>55</sup>

**Surface growth mechanism:** superoxide ( $\text{O}_2^-$ ) adsorbs on the cathode surface to produce  $\text{O}_{2\text{sur}}^-$  and then reacts with  $\text{Li}^+$  ions from the electrolyte to generate  $\text{LiO}_{2\text{sur}}$ .  $\text{LiO}_{2\text{sur}}$  is further reduced to generate  $\text{Li}_2\text{O}_2$  by a  $1\text{e}^-$  reduction step. The lower  $\text{LiO}_2$  solubility in the surface growth pathway results in the generation of thin-film  $\text{Li}_2\text{O}_2$  coating the surface, corresponding to a low capacity.



### 3. Descriptors for the catalytic activity of perovskite oxides

#### 3.1 $e_g$ filling

Shao-Horn *et al.*<sup>33</sup> established an  $e_g$ -filling theory to disclose the fundamental mechanism of the ORR in ABO<sub>3</sub>-type perovskites in alkaline solution. The d orbital of the central metal possesses two energy levels, namely,  $e_g$  and  $t_{2g}$  orbitals. Assuming that the surface transition metal center (B site) directly adsorbs O<sub>2</sub> molecules, the  $e_g$  orbital is predicted to overlap the O-2p<sub>σ</sub> orbital, and this overlap is stronger than that between the  $t_{2g}$  and O-2p<sub>π</sub> orbitals. Hence, compared to  $t_{2g}$ ,  $e_g$ -filling of the B site is considered a more suitable indicator for the bonding strength between the B site and oxygen. Fig. 2(e) shows a volcano plot demonstrating the ORR activity of perovskites as a function of  $e_g$ -filling. A moderate amount of  $e_g$ -filling close to 1 promises the highest ORR performance. Low  $e_g$ -filling is predicted to result in strong B–O<sub>2</sub> bonding, and high  $e_g$ -filling in weak O<sub>2</sub> interaction. Likewise, the same group proposed that an  $e_g$  occupation close to 1.2 and a high metal–oxygen covalency in perovskites contribute to optimized OER activity.<sup>32</sup> Fig. 2(f) depicts OER activity as a function of the occupancy of the  $e_g$ -symmetry electron site of the transition metal cation. Shao-Horn's principle highlights that optimizing  $e_g$  filling is a feasible approach for the design of highly active perovskite catalysts, such as LaCoO<sub>3</sub>,<sup>40,56</sup> SrNb<sub>0.1</sub>Co<sub>0.7</sub>Fe<sub>0.2</sub>O<sub>3-δ</sub>,<sup>57</sup> PrBa<sub>0.5</sub>Sr<sub>0.5</sub>Co<sub>1.5</sub>Fe<sub>0.5</sub>O<sub>5-δ</sub>,<sup>41</sup> and CaCu<sub>3</sub>Fe<sub>4</sub>O<sub>12</sub>.<sup>58</sup>

#### 3.2 Oxygen p-band center

The oxygen p-band center ( $O_p$ ) refers to the centroid of the PDOS of the O 2p orbit relative to the Fermi level (Fig. 2(g)), and is considered to be a bulk electronic structure descriptor for the evaluation of the catalytic activity of perovskites, based on density functional theory (DFT) calculations (Fig. 2(h)).<sup>50</sup> The gap value between the metal d-band center ( $M_d$ ) and  $O_p$ ,  $\Delta E_{d-p}$ , is qualitatively associated with the bond hybridization of oxygen and the transition metal (TM). The strong hybridization between the metal 3d and O 2p orbitals positively affects the ORR/OER activity.<sup>50</sup> One study suggests that the concentration of V<sub>o</sub> can influence both  $M_d$  and  $\Delta E_{d-p}$  in Sm<sub>0.5</sub>Sr<sub>0.5</sub>CoO<sub>3-δ</sub>.<sup>51</sup> The increased V<sub>o</sub> in Sm<sub>0.5</sub>Sr<sub>0.5</sub>CoO<sub>3-δ</sub> decreases the coordination number and valence state of Co (<4+), further affecting the magnetic moment of the perovskite. The relationship between  $\delta$  in Sm<sub>0.5</sub>Sr<sub>0.5</sub>CoO<sub>3-δ</sub> and its electronic structure was revealed as an association between the V<sub>o</sub> concentration and ORR/OER performance (Fig. 2(i)). Both experimental and DFT results suggest that the ORR can be enhanced by lifting the  $M_d$  close to the Fermi level, and OER can be boosted by decreasing  $\Delta E_{d-p}$ , which can be tuned by the generation of V<sub>o</sub> in the perovskite (Fig. 2(j) and (k)). Altogether, ORR and OER activity is strengthened by reducing  $\Delta E_{d-p}$ , which can be realized by increasing  $M_d$ . More interestingly, the closer V<sub>o</sub> is to the perovskite surface, the greater the promotion effect on catalytic activity (Fig. 2(l)). However, the fundamental mechanism of the ORR/OER of perovskites in a nonaqueous solution has not yet been fully understood.

#### 3.3 Lattice oxygen

In addition to the B-site metal cationic redox contribution to the catalytic activity of perovskites, lattice oxygen on or near the perovskite surface is regarded as another redox pair that participates in the OER.<sup>59–62</sup> Grimaud *et al.*<sup>60</sup> predicted that when the O 2p orbit center moves up towards the Fermi level, the oxidation of lattice oxygen in perovskite oxides is thermodynamically favorable. Perovskite oxides with lattice-oxygen participation also demonstrate pH-dependent OER activity, implying a non-cooperative proton–electron transfer process.<sup>60</sup> Pan *et al.*<sup>63</sup> prepared Si-doped SrCoO<sub>3-δ</sub> (Si-SCO), which showed better OER performance at different pH conditions than SCO (Fig. 3(a) and (b)). The lattice-oxygen oxidation mechanism (LOM) together with the adsorbate evolution mechanism (AEM) reaction pathways on Si-SCO are illustrated in Fig. 3(c), in which the LOM indicates that oxygen atoms on perovskites directly serve as active sites in the OER, and that AEM occurs through a concerted proton-coupled electron-transfer process on transition metal moieties. The contribution from the LOM to the OER activity of bulk perovskites was superior to that from the AEM. Notably, the influence of lattice oxygen from the perovskite surface resulted in a surface vacancy, and the generated vacant site was refilled by oxygen anions moving from the bulk material. The intrinsic OER activity was highly related to the diffusion rate of oxygen ions. A higher replenishment speed of surface lattice oxygen was responsible for a fast ion-diffusion rate, which benefited high OER activity (Fig. 3(d)). Si-SCO based on the LOM mechanism underwent surface reconstruction after cycling, as revealed by high-resolution transmission electron microscopy (HR-TEM) images (Fig. 3(e)), verifying the possible participation of lattice-oxygen redox.

In nonaqueous solutions, oxygen sites on the catalyst surface can directly interact with Li<sup>+</sup> ions from the electrolyte to generate surface Li sites, promoting the growth of Li<sub>2</sub>O<sub>2</sub>.<sup>17</sup> To illustrate the influence of both cation and anion redox on ORR/OER activity, our group prepared LaMnO<sub>3</sub> (LMO) perovskites with different surface atomic arrangements, namely, La-terminated or Mn-terminated surfaces (Fig. 3(f)).<sup>61</sup> The d band of the TM approached the Fermi-level in Mn-terminated LMO, while the O p band was near the Fermi-level in La-terminated LMO (Fig. 3(g) and (h)). Mn-terminated LMO involvement in both anion redox (surface lattice-O redox) and cation redox (TM redox) reactions resulted in the generation of a film-like discharge product. La-terminated LMO was inactive toward O<sub>2</sub> adsorption because of the nearly void d bands of the La sites, while the Mn-terminated surface actively adsorbed both O<sub>2</sub> and Li ions. Owing to the exposed lattice O from the stretched metal–oxygen bond and the presence of Mn<sup>3+</sup> with a half-filled d band, the Mn-terminated LMO showed higher activity toward adsorbed O<sub>2</sub> than La-terminated LMO. Under air, the assembled LOB using an Mn-terminated LMO cathode exhibited superior performance than that using a La-terminated LMO (Fig. 3(i) and (j)).

Dynamic surface oxygen-involved reaction leads to an unstable surface, especially when the surface oxygen cannot



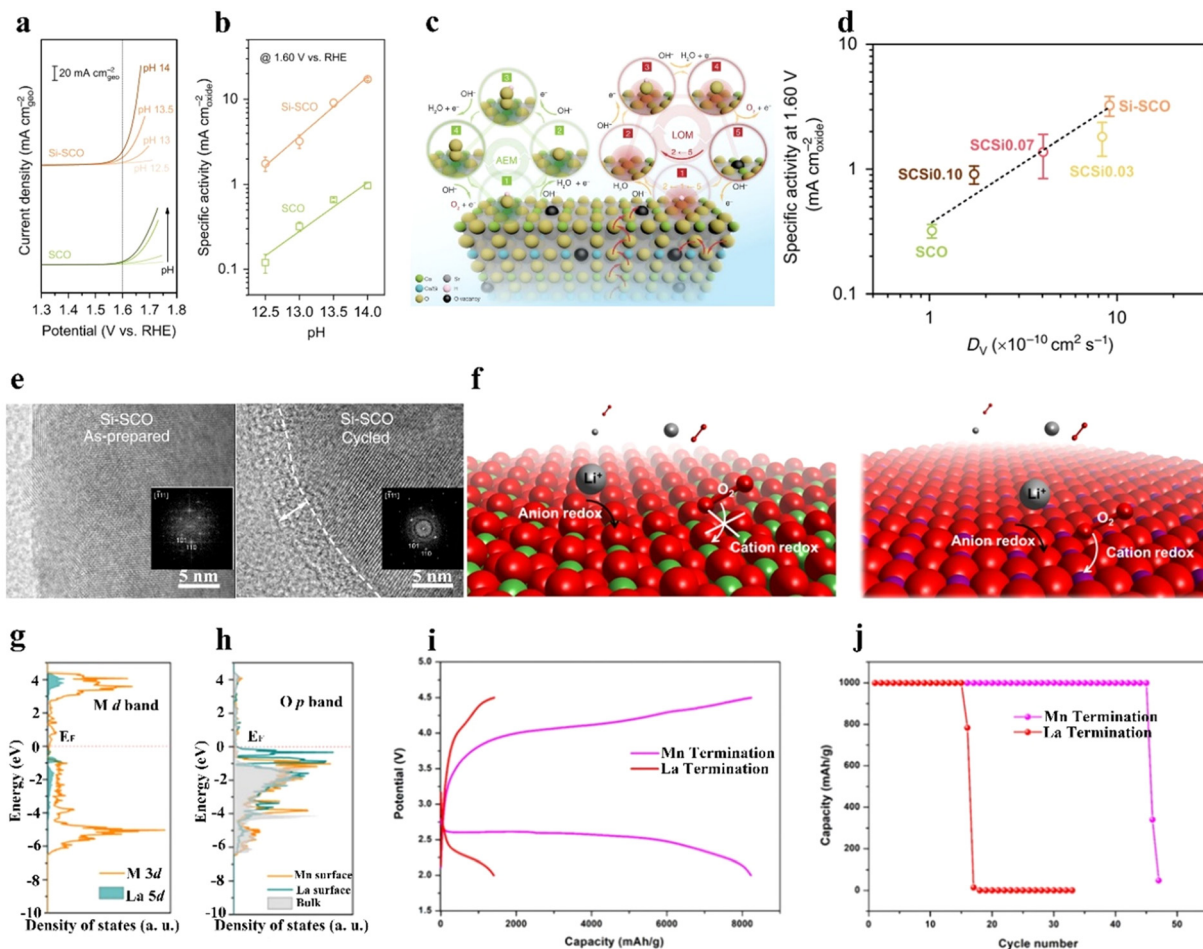


**Fig. 3** Lattice oxygen on or near the perovskite surface to participate in the OER. (a) OER current density, and (b) specific activity of Si-doped SCO and SCO under different pH conditions. (c) Schematic illustration of the AEM and LOM mechanisms on Si-doped SCO. (d) The relationship between OER and the diffusion rate of  $V_O$ . (e) HR-TEM images of Si-SCO before and after cycling. Insets: Corresponding fast Fourier transformed patterns. (a)–(e) Reproduced with permission.<sup>63</sup> Copyright 2020, Springer Nature. (f) Illustration of reactions on La- and Mn-terminated  $\text{LaMnO}_3$  surfaces. (g) The density of states of the Mn 3d and La 5d bands. (h) Oxygen 2p bands of Mn- and La-terminated  $\text{LaMnO}_3$ . (i) Discharge/charge curves at 200  $\text{mA g}^{-1}$ . (j) Cycling stability of Mn- and La-terminated  $\text{LaMnO}_3$  catalysts in a nonaqueous solution under air. (f)–(j) Reproduced with permission.<sup>61</sup> Copyright 2021, American Chemical Society.

be refilled by the bulk oxygen.<sup>63–65</sup> Hence, it is important to stabilize the perovskite surface to achieve high OER/ORR activity. Constant dissolution and deposition of catalysts during operando conditions may be a possible way to stabilize the catalyst surface, referred to as a self-healing process.<sup>63</sup>

## 4. Strategies for enhancing the catalytic activity of perovskites

Several tactics to promote the catalytic activity of perovskites are summarized in this mini-review, including dimensional control by synthetic methods, site substitution, oxygen vacancies, and perovskite-based composite catalysts. Table 1 lists the electrochemical performance and highlights of LOBs with perovskite cathodes.

### 4.1 Dimensional control by synthetic methods

Bulk perovskites show inferior stability and insufficient bifunctionality for the ORR/OER, giving rise to low specific capacities,

poor rate capability, inferior round-trip efficiencies, and cycling instability. Nanosizing the bulk perovskites effectively enlarges the interfacial contact between the electrolyte and catalyst and exposes more active sites for the ORR/OER.<sup>11,14,15,91</sup> Various nanostructures and morphologies of perovskites have been fabricated, including nanocrystals,<sup>66,92</sup> 0D nanospheres,<sup>75,83,86,93</sup> 1D nanofibers/nanotubes,<sup>25,71–73,78,82,94</sup> 2D nanosheets,<sup>76</sup> 3D ordered structures,<sup>85,95</sup> and nanocubes.<sup>96,97</sup> This mini-review summarizes the research on small- and large-sized perovskite catalysts for LOBs in recent years.

**4.1.1 Synthesis of small perovskites (<10 nm).** When the size of bulk perovskites is reduced to the nanoscale, a host of active sites can be exposed to considerably boost catalytic activity, and the surface electronic structure of perovskites can be tailored. In addition, the adsorption energy of  $\text{LiO}_2$  on the different facets of nanosized perovskite varies, which influences the OER performance.

$\text{CsPbBr}_3$  perovskite cubic nanocrystals ( $\sim 8.5$  nm) were prepared as catalysts for LOBs by a typical hot-injection strategy







Table 1 The electrochemical performance of LOBs with perovskite cathodes

| Perovskite  | Synthetic method                    | Structure  | Specific capacity (mA h g <sup>-1</sup> )           | Overpotential (V@mA h g <sup>-1</sup> )                     | Cycle life (cycles@mA h g <sup>-1</sup> )            | Highlights  | Ref. |
|---|-------------------------------------|--|---|---|--|---|------|
| CePbBr <sub>3</sub>   | Hot-injection method                | Cubic nanocrystal  | 7648@100  |   | 400@1000@500   |   | 66   |
| LaMnO <sub>3</sub>  | Electrospinning                     | Nanofiber  | 18 000@200  |   | 100@1000@200   | Collective anion and TM redox   | 61   |
| La <sub>0.7</sub> MnO <sub>3-δ</sub>  | Sol-gel                             | Nanoparticle   | 29 286@50   | 0.38@1000@200   | 375@1000@300   | A-site cationic defects   | 67   |
| S-doped LiNaO <sub>3</sub>  | Sol-gel                             | Nanoparticle   | 24 067@100  | 0.37@1000@200   | 347@1000@100   | Oxygen vacancy  | 68   |
| LaF <sub>3</sub> /La <sub>0.8</sub> Fe <sub>0.9</sub> Co <sub>0.1</sub> O <sub>3-δ</sub>                  | Sol-gel                             | Nanoparticle   | 7373.5@100  | 1.29@500@200  | 157@500@200  | F dopant  | 69   |
| Ni-doped LaNiO <sub>3</sub>   | Sol-gel                             | Nanoparticle   | 5910@50   | 0.9@500@250   | 50@500@250   | Oxygen vacancy  | 70   |
| Oxygen-defective CaMnO <sub>3</sub>   | Sol-gel                             | Interconnected nanoparticle  | 3600@250  | 1.0@500@500   | 114@500@500  | Redox mediator LiI; defects   | 45   |
| LaMn <sub>0.7</sub> Co <sub>0.3</sub> O <sub>3-δ</sub>  | Electrospinning                     | Nanofiber  | 13 019@400  | 0.81@1000@200   | 161@1000@200   | 1D nanotube structure   | 71   |
| La <sub>0.6</sub> Ca <sub>0.4</sub> Fe <sub>0.8</sub> Ni <sub>0.2</sub> O <sub>3</sub>                    | Electrospinning                     | Nanotube   | 12741.7@50  |   | 137@500@400  | 1D porous double-doped perovskite   | 72   |
| RuO <sub>2</sub> @La <sub>0.6</sub> Str <sub>0.4</sub> Co <sub>0.8</sub> Mn <sub>0.2</sub> O <sub>3</sub> | Electrospinning                     | RuO <sub>2</sub> nanosheets on nanofiber                                   |   | 1.32@500@50   | 100@500@50   | RuO <sub>2</sub> /perovskite composite  | 73   |
| CoO/Str <sub>0.5</sub> Y <sub>0.1</sub> CoO <sub>3-δ</sub>  | Electrospinning                     | Nanorod  | 3100@50   |   | 130@500@50   | CoO/perovskite composite  | 25   |
| La <sub>0.8</sub> Str <sub>0.2</sub> VO <sub>3</sub>  | Electrospinning                     | Porous nanotube  | 5800@2000   | 1.16@1000@100   | 253@1000@2000  | High reversibility under high current densities                                   | 42   |
| LaSrCoO/Ti <sub>3</sub> C <sub>2</sub> T <sub>x</sub>   | Hydrothermal                        | Perovskite nanoparticle on 2D nanosheet                                    | 11 340@500  | 1.02@1000@500   | 80@1000@500  | MXene/perovskite composite  | 27   |
| LaNi <sub>0.9</sub> Co <sub>0.1</sub> O <sub>3</sub>  | Hydrothermal                        | Nanosheet  |   | 1.5@1000@0.1 mA cm <sup>-2</sup>                            | 100@1000@0.1 mA cm <sup>-2</sup>                     | A binder-free electrode   | 74   |
| La <sub>0.8</sub> Str <sub>0.2</sub> Co <sub>0.8</sub> Fe <sub>0.2</sub> O <sub>3-δ</sub>                 | Sol-gel                             | Nanoparticle   | 26 833@50   | 0.55@1000@100   | 200@1000@300   | Adjust metal-O covalency  | 43   |
| LaCo <sub>0.75</sub> Mn <sub>0.25</sub> O <sub>3-δ</sub>  | Hydrothermal                        | Hollow spherical structure   | 10 301@200  | 1.15@500@200  | 60@500@200   | Tunable defect and surface structure  | 75   |
| LaFeO <sub>3-δ</sub>  | Sol-gel                             | 2D nanosheet   | 14 983@100  | 1.2@1000@100  | 60@1000@100  | Oxygen defects  | 76   |
| LaNi <sub>0.25</sub> Co <sub>0.75</sub> O <sub>3-δ</sub>  | Sol-gel                             | Interconnected nanoparticle  | 7720@0.1 mA cm <sup>-2</sup>                        |   | 49@1000  | Ni dopant   | 77   |
| Ni <sub>3</sub> S <sub>2</sub> /PrBa <sub>0.5</sub> Str <sub>0.5</sub> Co <sub>2</sub> O <sub>5+δ</sub>   | Electrospinning & ALD               | Ni <sub>3</sub> S <sub>2</sub> nanoparticle on hollow perovskite nanofiber | 12 874@100  | 0.68@1000@100   | 120@1000@100   | Metal sulfide/perovskite composite  | 78   |
| Fe <sub>2</sub> O <sub>3</sub> /LaNiO <sub>3</sub>  | Microwave & ALD                     | 2D nanosheet   | 10 419@100  | 0.77@1000@100   | 90@500@100   | Iron oxide/perovskite composite   | 79   |
| La <sub>0.6</sub> Str <sub>0.4</sub> Co <sub>0.2</sub> Fe <sub>0.8</sub> O <sub>3-δ</sub> @Pd             | Wet chemistry                       | Nanoparticle   | 16 912@200  |   | 38@500@200   | Pd/perovskite composite   | 80   |
| La <sub>0.8</sub> Fe <sub>0.9</sub> Co <sub>0.1</sub> O <sub>3-δ</sub>                                    | Sol-gel                             | Nanoparticle   | 7270.1@100  | 0.7 V@500@200   | 215@500@500  | Metal and alloy exsolution  | 81   |
| La <sub>0.75</sub> Str <sub>0.25</sub> MnO <sub>3</sub>   | Electrospinning                     | Porous nanotube  | 11 000@0.025 mA cm <sup>-2</sup>                    |   | 124@1000@0.15 mA cm <sup>-2</sup>                    | Hollow 1D channels beneficial for electron transport and O <sub>2</sub> diffusion | 82   |
| Sr-doped-La <sub>2</sub> NiO <sub>4</sub> /NiO  | Spray pyrolysis                     | Spherical particle   | 131 380@200   | 0.66@500@500  | 188@500@200  | Sr dopant   | 83   |
| LaNi <sub>0.5</sub> Co <sub>0.5</sub> O <sub>3</sub>  | Sol-gel                             | Spherical nanoparticle   | 7.96 mA h cm <sup>-2</sup> @0.1 mA cm <sup>-2</sup> | 0.05@0.5 mA cm <sup>-2</sup> @0.1 mA cm <sup>-2</sup>       | 100@0.5 mA cm <sup>-2</sup> @0.1 mA cm <sup>-2</sup> | 98.2% energy efficiency LOB   | 84   |
| LaFeO <sub>3-δ</sub>  | Emulsion polymerization & Annealing | 3D ordered macroporous honeycomb   | 15 000@0.025  |   | 124@1000@0.15 mA cm <sup>-2</sup>                    | 3D ordered macroporous structure  | 85   |
| La <sub>0.6</sub> Str <sub>0.4</sub> CoO <sub>3-δ</sub>   | Hydrothermal & template method      | Macrosphere  | 4895@100  | 1.06@100(non-capacity limit) 0.9@100@10 mA cm <sup>-2</sup> | 30@500@0.1 mA cm <sup>-2</sup>                       | Catalytic activity in both aqueous and non-aqueous solution                       | 86   |
| RuO <sub>2</sub> /La <sub>2</sub> LiRuO <sub>6-δ</sub>  | Ball milling                        | Nanoparticle   |   | 1.3@500@400   | 665@200@100  | Solid-state LOB   | 38   |
| Ag@La <sub>0.6</sub> Str <sub>0.4</sub> Fe <sub>0.9</sub> Mn <sub>0.1</sub> O <sub>3</sub>                | Sol-gel & UV irradiation            | Nanoparticle   | 12 477  |   | 147@500@400  | Ag/perovskite composite   | 87   |
| Ni-Lao <sub>0.9</sub> Mn <sub>0.6</sub> Ni <sub>0.4</sub> O <sub>3-δ</sub>                                | Electrospinning                     | Nanoparticles on nanofiber   | 16 656@400  |   | 95@500@400   | Exsolution of Ni nanoparticles  | 88   |
| LaCo <sub>0.8</sub> Fe <sub>0.2</sub> O <sub>3</sub> @rGO   | Hydrothermal                        | Nanowire on rGO sheet  | 7088.2@200  | 0.98@500@200  | 56@500@200   | rGO/perovskite composite  | 89   |
| α-Fe <sub>2</sub> O <sub>3</sub> /La <sub>0.8</sub> FeO <sub>3-δ</sub>                                    | Sol-gel                             | Nanoparticle   | 7183@100  | 1.0@500@100   | 108@500@100  | Fe <sub>2</sub> O <sub>3</sub> /perovskite composite                              | 90   |

Note: rGO: reduced graphene oxide.

(Fig. 4(a) and (b)).<sup>66</sup> During charging, the decomposition of  $\text{Li}_2\text{O}_2$  in the  $\text{CsPbBr}_3$  nanocrystals followed two steps: (1)  $\text{Li}_2\text{O}_2 = \text{LiO}_2 + \text{Li}^+ + \text{e}^-$  and (2)  $\text{LiO}_2 = \text{O}_2 + \text{Li}^+ + \text{e}^-$  (rate-determining step), as shown in Fig. 4(c). The (100) facet displayed the smallest adsorption energy toward  $\text{LiO}_2$  compared to the (110), (210), (211), and (321) facets, resulting in a small overpotential for the OER. For the ORR process,  $\text{LiO}_2$  preferentially dissolved in the electrolyte and produced the toroid-type  $\text{Li}_2\text{O}_2$  based on the solution growth mechanism (Fig. 4(d)). Additionally,  $\text{CsPbBr}_3$  perovskite quantum dots (4–5 nm) were deposited into an iron-based metal–organic framework in organic solvent *via* a sequential deposition

method, named  $\text{CsPbBr}_3@\text{PCN-333}(\text{Fe})$  (Fig. 4(e) and (f)).<sup>92</sup> Oleic acid and oleylamine were added to the mixture as organic stabilizers. The composite was applied as a photoelectric cathode for a light-assisted LOB. The LOB using the  $\text{CsPbBr}_3@\text{PCN-333}(\text{Fe})$  cathode retained a higher discharge voltage (2.5 V at  $0.5 \text{ mA cm}^{-2}$ ) than  $\text{CsPbBr}_3$  (<2 V) and  $\text{PCN-333}(\text{Fe})$  (2.4 V) (Fig. 4(g)).

#### 4.1.2 Synthesis of large perovskites

**Sol-gel.** Sol-gel is a facile synthetic method used to prepare perovskite nanomaterials based on the inorganic polymerization reaction of molecular precursors.<sup>26,43,45,67–70,84,98–100</sup> First, different metal nitrates or acetates with specific stoichiometric

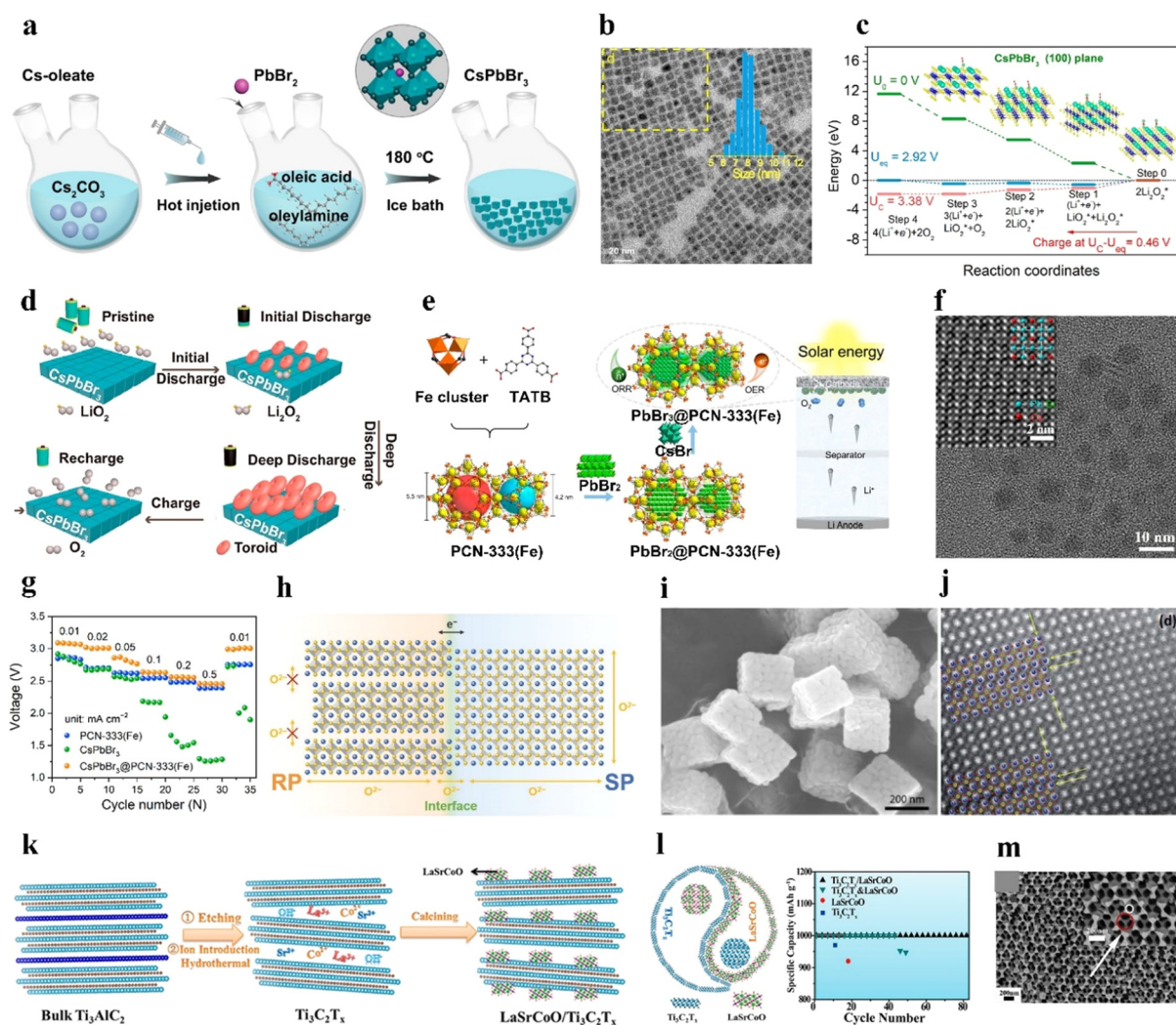


**Fig. 4** Synthesis of large perovskites. (a) Illustration of the synthesis process of  $\text{CsPbBr}_3$  nanocrystals. (b) Transmission electron microscopy (TEM) image of  $\text{CsPbBr}_3$  nanocrystals. (c) Gibbs free energy at different potentials of  $\text{CsPbBr}_3$ . (d) Demonstration of discharging/charging processes for LOBs with  $\text{CsPbBr}_3$ . (a)–(d) Reproduced with permission.<sup>66</sup> Copyright 2021, American Chemical Society. (e) Preparation process of  $\text{CsPbBr}_3@\text{PCN-333}(\text{Fe})$ . (f) TEM image of  $\text{CsPbBr}_3@\text{PCN-333}(\text{Fe})$ . (g) Variation of discharge voltage at distinct current densities with  $\text{CsPbBr}_3@\text{PCN-333}(\text{Fe})$  and control samples under illumination. (e)–(g) Reproduced with permission.<sup>92</sup> Copyright 2021, American Chemical Society. (h) Demonstration of the possible electron and oxygen-ion transfer at the interface of dual phases in  $\text{LaSr}_{3-y}$ . Reproduced with permission.<sup>101</sup> Copyright 2021, Wiley-VCH. (i) Scanning electron microscopy (SEM) image of  $\text{La}_{0.9}\text{Co}_{0.8}\text{Ni}_{0.2}\text{O}_{3-x}$  nanocubes. Reproduced with permission.<sup>97</sup> Copyright 2019, Elsevier. (j) Scanning TEM image of  $\text{LaNi}_{0.9}\text{Cu}_{0.1}\text{O}_3$  with crystal strains. Reproduced with permission.<sup>74</sup> Copyright 2017, Royal Society of Chemistry. (k) Illustration of the synthesis process of the  $\text{LaSrCoO}/\text{Ti}_3\text{C}_2\text{T}_x$  composite. (l) Cycling stability of  $\text{LaSrCoO}/\text{Ti}_3\text{C}_2\text{T}_x$ . Reproduced with permission.<sup>27</sup> Copyright 2019, American Chemical Society. (m) SEM image of macroporous  $\text{LaMnO}_3$ . Reproduced with permission.<sup>95</sup> Copyright 2019, Elsevier.





ratios are dissolved in deionized water, followed by adding chelating agents (e.g., ethylenediamine tetraacetic acid and citrate acid) and binding agents (like ethylene glycol). An  $\text{NH}_4\text{OH}$  solution is added to the above mixture to adjust the pH of the mixture to 6–8, allowing complete complexation. Then, the mixture is aged at 80–120 °C to form a gel. The gel is further dried below 300 °C to generate a fluffy resultant, followed by high-temperature annealing (above 600 °C) under air to remove organic moieties. The sol-gel approach combined with ultraviolet light was used to place Ag nanoparticles on  $\text{La}_{0.6}\text{Sr}_{0.4}\text{Fe}_{0.9}\text{Mn}_{0.1}\text{O}_3$  with a BET specific surface area (SSA) of  $20.83 \text{ m}^2 \text{ g}^{-1}$ . The derived LOB exhibited a superior capacity ( $12\,477 \text{ mA h g}^{-1}$  at  $400 \text{ mA g}^{-1}$ ) and a long cycle life (147 cycles under a limited capacity of  $500 \text{ mA h g}^{-1}$  at  $400 \text{ mA g}^{-1}$ ).<sup>87</sup>

$\text{V}_o$  can be created by annealing the perovskite product derived from the sol-gel under a reducing atmosphere such as an  $\text{H}_2/\text{Ar}$  mixed atmosphere.<sup>45</sup> Zhu *et al.*<sup>100</sup> prepared  $\text{La}_{1-x}\text{FeO}_{3-\delta}$  perovskites with surface  $\text{V}_o$  and a small portion of  $\text{Fe}^{4+}$  species, as bifunctional ORR/OER catalysts by an EDTA-citrate complexing sol-gel process. In addition, Xu *et al.*<sup>101</sup> used a sol-gel method to prepare cation-deficient  $\text{LaSr}_{3-y}$  with dual phases of Ruddlesden-Popper perovskite (RP) and single perovskite (SP) with controllable structures and compositions. The interfacial interaction of the perovskite composite elevated the oxygen and ionic transport, which enhanced the lattice-O participation in the OER process in an alkaline electrolyte (Fig. 4(h)).

Oxygen in sol-gel derived perovskite oxides can be replaced by N, S, and F, which is realized by placing anion precursors and the perovskite oxide in two separated porcelain boats in a tube furnace, followed by heating at around 300–400 °C under an Ar atmosphere.<sup>68,69</sup> In short, the sol-gel method allows flexibility in the construction of various perovskites. However, perovskite oxides prepared by this method generally possess a low BET surface area ( $< 50 \text{ m}^2 \text{ g}^{-1}$ ), unfavorable for electrolyte diffusion and limiting the number of exposed active sites.

**Electrospinning.** 1D perovskite nanofibers with high surface-to-volume ratios show a relatively large surface area and well-distributed porosity, which maximizes the electrolyte-accessible active sites, facilitates mass transport, accommodates reaction products, and mitigates the clogging issue on the catalyst surface. An electrospinning method has been widely adopted to prepare 1D porous perovskite nanomaterials, such as  $\text{La}_{0.6}\text{Ca}_{0.4}\text{Fe}_{0.8}\text{Ni}_{0.2}\text{O}_3$ ,  $\text{LaMn}_{0.7}\text{Co}_{0.3}\text{O}_{3-x}$  nanotubes,  $\text{PrBa}_{0.5}\text{Sr}_{0.5}\text{Co}_{2-x}\text{Fe}_x\text{O}_{5+\delta}$  nanofibers,  $\text{La}_{0.6}\text{Sr}_{0.4}\text{Co}_{0.8}\text{Mn}_{0.2}\text{O}_3$  nanofibers,  $\text{Sr}_{0.9}\text{Y}_{0.1}\text{CoO}_{3-\delta}$  nanorods, and  $\text{La}_{0.8}\text{Sr}_{0.2}\text{VO}_3$  nanofibers.<sup>25,42,71–73,102</sup> First, one or more metal precursors are dissolved in organic solvent and mixed with polymer solutions like polyacrylonitrile and polyvinylpyrrolidone (PVP) to generate the mother solution. Then, the mixture is filled into a plastic syringe tube equipped with a stainless-steel nozzle. The solution is electrospun onto a rotating drum, as a collector, under a high voltage. Thereafter, the collected nanofibers are stabilized and pyrolyzed in a muffle oven or tube furnace.

The morphology and porous structure of the electrospinning products can be tailored using different amounts of polymer precursors during electrospinning. As such, Wang *et al.*<sup>72</sup> demonstrated that adjusting the concentration of PVP changed the morphology of  $\text{La}_{0.6}\text{Ca}_{0.4}\text{Fe}_{0.8}\text{Ni}_{0.2}\text{O}_3$  from nanofiber to nanotube. A low concentration of PVP, around  $0.13 \text{ g mL}^{-1}$ , resulted in the formation of hollow nanotubes with a diameter of 100–200 nm, while a higher-concentration of PVP of around  $0.18 \text{ g mL}^{-1}$  generated solid nanofibers after calcination. When PVP was present in a low amount, it preferentially lied at the perovskite core to form a hollow structure. Although, the metal composition, morphology and porous structure of the resultant can be tuned by adopting various precursor components and annealing temperatures, the distribution of multi-scale pores cannot be realized by the electrospinning technique.

**Hydrothermal.** A hydrothermal method has been used to prepare perovskites or their composites as effective catalysts for LOBs.<sup>27,74,97</sup> Sun *et al.*<sup>97</sup> prepared porous  $\text{La}_{0.9}\text{Co}_{0.8}\text{Ni}_{0.2}\text{O}_{3-x}$  nanocubes by a hydrothermal method in the presence of PVP and glycine. The nanocubes had a larger BET surface area ( $23.45 \text{ m}^2 \text{ g}^{-1}$ ) than that of the sample prepared by the sol-gel process ( $4.82 \text{ m}^2 \text{ g}^{-1}$ ) (Fig. 4(i)). PVP and glycine, as a potential crystal face inhibitor and shape-control agent, respectively, were applied to produce the cube-like framework.

A binder-free electrode is conducive for effective electron transfer. As such,  $\text{LaNi}_{0.9}\text{M}_{0.1}\text{O}_3$  (M: Cu or Co) perovskite nanosheets were deposited on 3D Ni foam by a hydrothermal method as self-standing air electrodes for LOBs, and the derived sample exhibited an SSA of  $240 \text{ m}^2 \text{ g}^{-1}$ .<sup>74</sup> Substituting  $\text{Ni}^{3+}$  with  $\text{Cu}^{2+}$  increased the crystalline plate distance and generated  $\text{V}_o$ . Crystal strain and dislocation defects can be observed in  $\text{LaNi}_{0.9}\text{Cu}_{0.1}\text{O}_3$  (Fig. 4(j)), attributed to the substitution with a TM ion of a different size, as well as the formation of  $\text{V}_o$  induced by the different chemical valence of the metal ions. Due to the microporous structure of the  $\text{LaNi}_{0.9}\text{Cu}_{0.1}\text{O}_3$  catalyst and the use of a redox mediator (tetrathiafulvalene), the derived LOB exhibited a small overpotential of 0.72 V and high round-trip efficiency.  $\text{Li}_2\text{O}_2$  was uniformly deposited on the catalyst nanosheet during the discharge process and then decomposed after the charging process. Moreover,  $\text{La}_{0.5}\text{Sr}_{0.5}\text{CoO}_{3-\delta}$  (LaSrCoO) nanoparticles were deposited in  $\text{Ti}_3\text{C}_2\text{T}_x$  nanosheets by hydrothermal and post-thermal treatment (Fig. 4(k)).<sup>27</sup> The LaSrCoO/ $\text{Ti}_3\text{C}_2\text{T}_x$  composite showed longer cycle life compared to LaSrCoO and  $\text{Ti}_3\text{C}_2\text{T}_x$  due to the synergistic effect of the dual components (Fig. 4(l)).

Since solid discharge products deposit on the surface of the catalysts, a porous structure of catalyst is essential for improving the electrochemical performance of LOBs. Macropores provide sufficient space for efficient mass diffusion ( $\text{Li}^+$  ions and  $\text{O}_2$ ), allowing fast ORR/OER kinetics. Mesoporous channels can trap the  $\text{Li}_2\text{O}_2$  discharge product and prevent it from diffusing into the electrolyte, ensuring favorable interfacial contact between  $\text{Li}_2\text{O}_2$  and the catalyst and thus lowering the reaction overpotentials.<sup>54</sup> Hard template synthesis,<sup>83,95</sup> a soft-template route,<sup>76</sup> and wet-chemistry<sup>80</sup> have been used to



prepare porous perovskites. Ordered macroporous  $\text{LaMnO}_3$  with an SSA of  $20.3 \text{ m}^2 \text{ g}^{-1}$  was prepared using PMMA colloidal crystals as a hard template, facilitating both oxygen and electrolyte diffusion (Fig. 4(m)).<sup>95</sup> However, only a few reports investigate how the porous structure and porosity influence the catalytic activity of perovskites for LOBs. Hence, more efforts are needed to investigate the property-activity relationship of perovskite catalysts.

## 4.2 A/B-O-site regulation in $\text{ABO}_3$

**4.2.1 A-site cation deficiency.** A/B-site cations can be substituted for other cations with different valences or radii. The adjustment of A-site cation size influences the chemical balance state of  $\text{ABO}_3$ , and results in the octahedron distortion in the initial cubic framework, generating cation vacancies or oxygen vacancies.<sup>47</sup> Owing to their unique structures, perovskites with diverse compositions demonstrate varying redox and surface properties. The order of ORR performance of  $\text{ABO}_3$  perovskites with disparate rare-earth metals as A-site elements was demonstrated to be  $\text{La} > \text{Pr} > \text{Nd} > \text{Sm} > \text{Gd} > \text{Y} > \text{Dy} > \text{Yb}$ .<sup>103</sup>

Perovskites with A-site vacancies can be prepared by a nonstoichiometric method. Du *et al.*<sup>67</sup> produced La defects in  $\text{La}_{0.7}\text{MnO}_{3-\delta}$  ( $\text{L}_{0.7}\text{MO}$ ) as a bifunctional catalyst for the OER/ORR by decreasing the stoichiometric ratio of  $\text{La}(\text{NO}_3)_3 \cdot 6\text{H}_2\text{O}$  in the sol-gel synthesis. The defective sample possessed a larger BET surface area ( $34.7 \text{ m}^2 \text{ g}^{-1}$ ) and pore size (20.6 nm) than that of the defective-free sample ( $11.9 \text{ m}^2 \text{ g}^{-1}$ , 8.9 nm), beneficial for oxygen and  $\text{Li}^+$  transport and the storage of  $\text{Li}_2\text{O}_2$ . The generated La defects effectively elevated the Mn-O bond covalency, which optimized the  $e_g$  electron filling state of the Mn ions and improved the overlapping status of Mn 3d and O 2p orbitals. Furthermore, La defects on the  $\text{L}_{0.7}\text{MO}$  surface served as multiple unsaturated active spots to adsorb oxygen intermediates, leading to strong interaction between the catalyst and  $\text{LiO}_2$ . Thereafter, the adsorbed  $\text{LiO}_2$  underwent a one-electron transfer reaction to generate a film-like  $\text{Li}_2\text{O}_2$  uniform covering on the catalyst surface, which corresponded to a surface growth mechanism. As a result, lattice-oxygen redox reactions and electron transfer in  $\text{La}_{0.7}\text{MnO}_{3-\delta}$  were accelerated between Mn and oxygen adsorbates. The LOB using  $\text{L}_{0.7}\text{MO}$  delivered a superior capacity of  $29\,286 \text{ mA h g}^{-1}$  at a current density of  $50 \text{ mA g}^{-1}$  (compared with  $13\,709 \text{ mA h g}^{-1}$  from the cell using a defective-free sample), a small voltage gap (0.38 V) and stable cycling life (375 cycles under a confined capacity of  $1000 \text{ mA h g}^{-1}$  at  $300 \text{ mA g}^{-1}$ ).

**4.2.2 B-site substitution.** The multiple oxidation states of the B site enable perovskites with tailorable surface redox properties, allowing their catalytic activity for chemical reduction or oxidation. B-site cations directly bond with oxygen-related adsorbates, and the degree of B-O<sub>2</sub> covalency can be altered by substituting the B-site with foreign cations. The radius, alkalinity or acidity, oxidation valence, and spin state of B-site metal ions impact the physicochemical properties and stability of the resulting perovskite.<sup>47</sup> Moreover, the

oxidation state and spin state of B-site cations can greatly influence their  $e_g$  electronic state.<sup>100</sup>

Owing to the overlap between B-site ions and the  $\text{O}^{2-}$  orbital, the electronic conductivity is governed by B-O-B bonds and the valence transition of the B cations.<sup>47</sup> A shorter B-B distance is conducive to the formation of O-O bonds between the neighboring adsorbates, beneficial for OER kinetics.<sup>104</sup> A shorter B-B bond in  $\text{ABO}_3$  and a smaller B-O-B angle can be realized by foreign-cation doping.<sup>105</sup> As such, doping a Co element into  $\text{LaMn}_{0.7}\text{Co}_{0.3}\text{O}_{3-x}$  nanotubes shortened the Mn-Mn distance and promoted the formation of O-O bonds, favorable for promoting the OER performance.<sup>71</sup> The assembled LOB could be operated for 161 cycles with a confined capacity of  $1000 \text{ mA h g}^{-1}$  at  $200 \text{ mA g}^{-1}$ .

Furthermore, the oxidation state of the B-site TM and the amount of  $\text{V}_o$  can be regulated by foreign-cation doping, providing a versatile way to correlate physicochemical features with catalytic activity. The presence of aliovalent dopants results in the generation of a positively charged  $\text{V}_o$  to maintain charge neutrality based on Coulomb's law. Defective perovskite structures assist in the migration, emission, and intercalation of lattice oxygen, thereby enhancing the redox capability of B-site cations. For example, the introduction of Sr decreases the valence state of the B-site metal and the crystallinity structure.<sup>42</sup> Sung *et al.*<sup>42</sup> induced a phase transition from  $\text{La}_{0.8}\text{Sr}_{0.2}\text{VO}_4$  monazite (LSV4) to  $\text{La}_{0.8}\text{Sr}_{0.2}\text{VO}_3$  perovskite (LSV3) under a reducing atmosphere (Fig. 5(a)). LSV3 showed a defective and porous structure, strain and lattice shrinkage induced by mismatching of  $\text{VO}_6$  octahedra (Fig. 5(b)). The reduced oxidation state from  $\text{V}^{5+}$  to  $\text{V}^{3+}$  induced by the Sr dopant allowed the generation of enriched  $\text{V}_o$  active sites. LSV3 exhibited better ORR and OER performance (Fig. 5(c) and (d)), conducive to the formation and decomposition of  $\text{Li}_2\text{O}_2$ . Accordingly, the assembled LOB demonstrated high reversibility over 253 cycles with a limited capacity of  $1000 \text{ mA h g}^{-1}$  at  $2000 \text{ mA g}^{-1}$  and stable rate capabilities at different current densities from 100 to  $2000 \text{ mA g}^{-1}$  (Fig. 5(e)).

In  $\text{LaCoO}_3$ , partial replacement of the Co site in the B-site with Mn or Fe can boost the rate kinetics and coulombic efficiency and elongate the cycle life of the resulting LOB. Abundant  $\text{V}_o$  in mesoporous  $\text{LaCo}_{0.75}\text{Mn}_{0.25}\text{O}_{3-\sigma}$  (LCMO) effectively bound the intermediate product of  $\text{Li}_{2-x}\text{O}_2$ , accelerated electron transfer, and lowered the reaction energy barrier.<sup>75</sup> Accordingly, the LOB using an LCMO cathode exhibited a low potential of 1.12 V and a high specific capacity of  $10\,301 \text{ mA h g}^{-1}$  at  $200 \text{ mA g}^{-1}$ . In another example, the doping effect of different cations like Mn and Fe in the catalytic activity of  $\text{La}_{0.6}\text{Sr}_{0.4}\text{CoO}_3$  was compared (Fig. 5(f)).<sup>106</sup> The Fe dopant was effective in reducing the grain size of the perovskite nanoparticles, leading to a higher SSA ( $10.69 \text{ m}^2 \text{ g}^{-1}$ ) than that of the pristine sample ( $6.68 \text{ m}^2 \text{ g}^{-1}$ ) and thus exposing more active sites. Moreover, the introduced  $\text{Fe}^{2+}$  contributed to generating more  $\text{V}_o$ , according to  $\text{Fe}_{\text{Fe}}^{\times} + \text{O}_o^{\times} \leftrightarrow \text{Fe}_{\text{Fe}}' + \text{V}_o^{\bullet} + \frac{1}{2}\text{O}_2$ . Mn possessed a mixed valence between  $2^{+}/3^{+}$  and  $3^{+}/4^{+}$ , and exhibited an electron-donating feature. Thus, the electron-rich Mn-doped



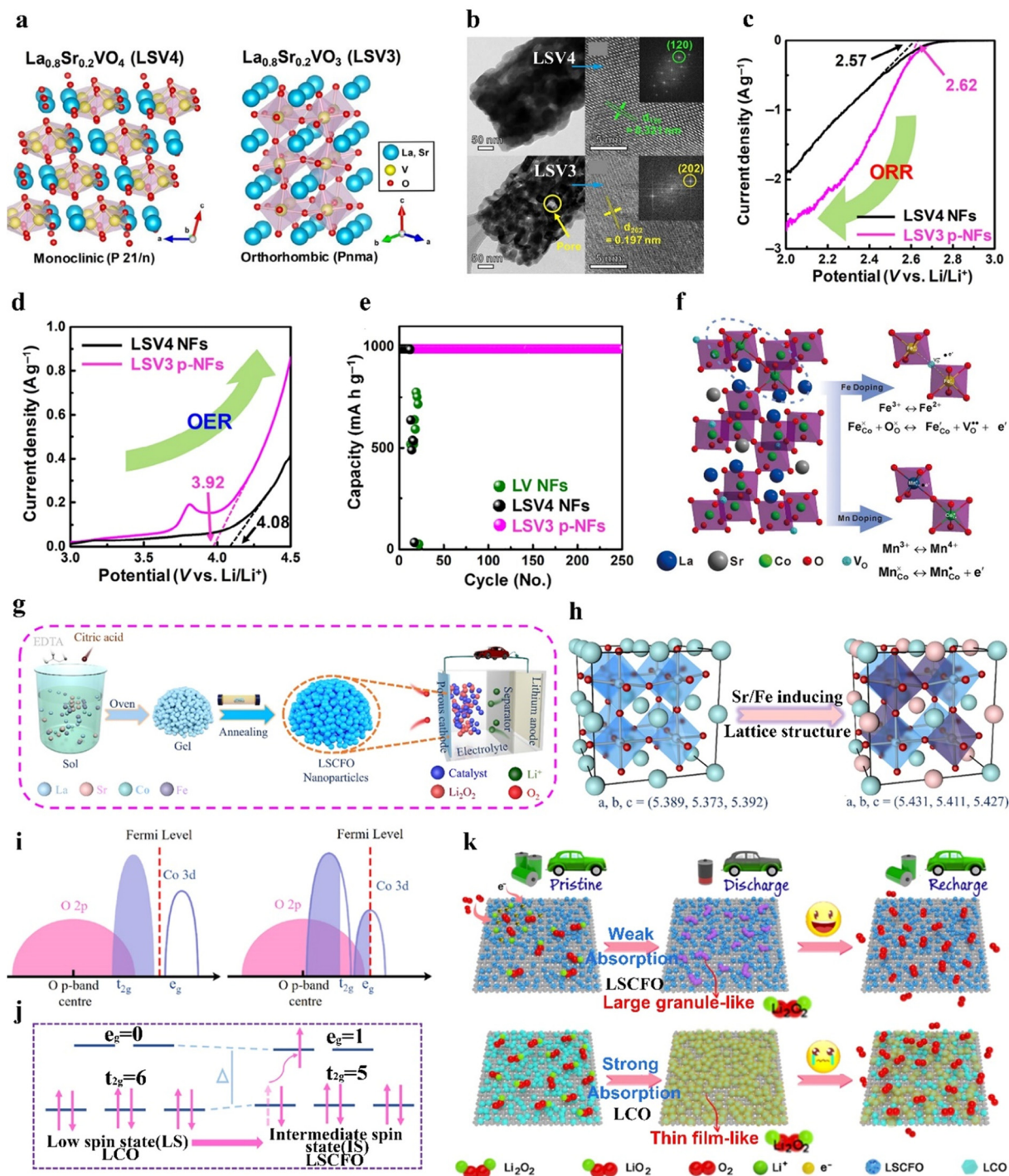


**Fig. 5** The impact of B-site substitution on perovskites. (a) Crystal structures of LSV4 and LSV3. (b) Low- and high-resolution TEM images of LSV4 and LSV3. (c) ORR and (d) OER linear sweep voltammetry of LSV4 and LSV3 at 5 mV s<sup>-1</sup>. (e) Cycling stability of LOBs with LSV4 and LSV3 catalysts. (a)–(e) Reproduced with permission.<sup>42</sup> Copyright 2021, Wiley-VCH. (f) Demonstration of the Fe and Mn dopants in La<sub>0.6</sub>Sr<sub>0.4</sub>CoO<sub>3</sub>. Reproduced with permission.<sup>106</sup> Copyright 2018, Wiley-VCH. (g) Schematic illustration of the preparation of LSCFO. (h) Crystal structures, and (i) the overlapping state of the Co 3d–O 2p bonds of LCO and LSCFO. (j) Schematic illustration of the spin state transformation from LCO to LSCFO. (k) Illustration of the oxygen electrode reaction pathways of LCO and LSCFO. (l) Illustration of the oxygen electrode reaction pathways of LCO and LSCFO. (g)–(k) Reproduced with permission.<sup>43</sup> Copyright 2021, American Chemical Society.

sample increased the electrical conductivity, which was beneficial for electron transfer during the ORR/OER. Mn and Fe dopants with larger radii than Co can expand the crystalline structure, and thus create more pathways for Li<sup>+</sup> transport. In

addition to a TM dopant, a magnesium dopant in LaNi<sub>1-x</sub>Mg<sub>x</sub>O<sub>3</sub> has been introduced to replace Ni, and this suppressed the formation of low-valence Ni<sup>2+</sup> ions ( $e_g > 1$ ). The presence of Ni<sup>3+</sup> ( $e_g = 1$ ) in the Mg-doped sample ensured





high ORR/OER activity.<sup>107</sup> The derived LOB with the Mg-doped cathode demonstrated a higher discharge capacity than that using the pristine sample.

Dual cation dopants in ABO<sub>3</sub> perovskites can synergistically regulate the adsorption capability of catalysts toward the LiO<sub>2</sub> intermediate and the morphology of the discharge product. LaCoO<sub>3</sub> (LCO) is a nonmagnetic insulator due to the low-spin state of Co<sup>3+</sup> with an atomic configuration of t<sub>2g</sub><sup>6</sup>e<sub>g</sub><sup>0</sup>.<sup>43</sup> Sr and Fe cations doped in porous LaCoO<sub>3</sub> perovskite nanoparticles (LSCFO) by a sol-gel method resulted in the formation of abundant V<sub>o</sub> and enhanced Co 3d–O 2p covalency bonds, and induced the transformation of Co<sup>3+</sup> from a low-spin state to an intermediate-spin state (Fig. 5(g)–(j)).<sup>43</sup> The enhanced Co 3d–O 2p covalency facilitated electron transfer between the surface TM and adsorbed intermediates, and the optimized spin state transformed the perovskite from a nonconductor state to a metallic state. Hence, the produced granule-like Li<sub>2</sub>O<sub>2</sub> in LSCFO can be more effectively decomposed during the charging process, compared to LCO (Fig. 5(k)). This LOB device demonstrated long-term cycling stability over 200 cycles at 300 mA g<sup>−1</sup>, and an ultrahigh specific capacity of 26 833 mA h g<sup>−1</sup> at 50 mA g<sup>−1</sup>. Moreover, Cu with a low valence state and Co with a favorable 4e<sup>−</sup> process were also co-doped to LaMnO<sub>3</sub> by gel combustion to promote ORR/OER activity.<sup>108</sup>

**4.2.3 O-site substitution.** Substituting the oxygen in ABO<sub>3</sub> perovskites by anions with relatively low Pauling electronegativity effectively strengthens the covalent characteristics of metal–anion bonds, thus reducing the bandgap. The decreased bandgap excites charge carriers to the conduction band, considerably boosting electronic conductivity. A sulfur dopant in perovskites contributes to the strengthened hybridization of the 3d orbital of the B-site cation and the 2p orbital of the O, which reinforces the bond strength and thereby boosts the catalytic kinetics.<sup>68,109,110</sup> For example, Long *et al.*<sup>68</sup> synthesized S-doped and O-defective LiNiO<sub>3</sub> (S-V<sub>o</sub>-LNO) with a narrow bandgap, and increased the electron-occupied state to nearer the Fermi level than in the pristine LNO. Furthermore, the upshift of the Ni 3d band center and downshift of the O 2p band center led to a smaller distance between them (Fig. 6(a)). The strengthened hybridization of Ni 3d and O 2p orbitals and the promoted Ni–O covalency boosted the electron transfer. In addition, Ni<sup>3+</sup> with an optimal e<sub>g</sub> orbital (t<sub>2g</sub><sup>6</sup>e<sub>g</sub><sup>1</sup>) was predicted to have a higher catalytic activity than that of Ni<sup>2+</sup> (t<sub>2g</sub><sup>6</sup>e<sub>g</sub><sup>2</sup>) according to e<sub>g</sub>-filling theory. A higher amount of Ni<sup>3+</sup> in S-V<sub>o</sub>-LNO compared to that in LNO increased the adsorption strength of oxygen intermediates on the surface and reduced the reaction energy barrier during the OER and ORR (Fig. 6(b) and (c)). The discharge products, Li<sub>2</sub>O<sub>2</sub> and Li<sub>2</sub>CO<sub>3</sub>, could be effectively decomposed on the surface of S-LNO after recharging, while they remained on the LNO surface. Consequently, the LOB using the S-LNO cathode exhibited a superior capacity of 24 067 mA h g<sup>−1</sup> at 100 mA g<sup>−1</sup>, low overpotential (0.37 V), favorable rate capability, and long cycle life (347 cycles with a limited capacity of 1000 mA h g<sup>−1</sup> at 100 mA g<sup>−1</sup>) (Fig. 6(d) and (f)).

Regulating the morphology and composition of the discharge product Li<sub>2</sub>O<sub>2</sub> is a feasible way to improve the

performance of LOBs, and can be realized by anion doping in perovskites. Using fluorine, the dopant with the highest electronegativity (4.0), can improve the electronic conductivity of electrocatalysts and generate V<sub>o</sub> by forming metal–F bonds. As shown in Fig. 6(g), Hou *et al.*<sup>69</sup> introduced an F dopant into La<sub>0.8</sub>Fe<sub>0.9</sub>Co<sub>0.1</sub>O<sub>3−δ</sub> (LFCO), reconstructing the surface property, manipulating the electronic structure, and tailoring the discharge reaction pathway of the LOB. The F dopant distorted the crystalline structure, increased the disorder degree in the adjacent environment of the Fe–O bond, and tailored the Fe/Co–O orbital hybridization. Based on theoretical calculations, due to the strong LiO<sub>2</sub> adsorption energy in the derived LaF<sub>3</sub>/LFCO composite, the discharge reaction process on the cathode followed the surface growth mechanism. In this context, LiO<sub>2</sub> may not transport to the electrolyte and may instead favor the formation of small-sized Li<sub>2</sub>O<sub>2</sub> (0.2 μm) in LaF<sub>3</sub>/LFCO, while the sample without F demonstrates larger-sized Li<sub>2</sub>O<sub>2</sub> (2 μm) that leads to a larger overpotential (Fig. 6(h) and (i)). The generated petal-like F-doped Li<sub>2</sub>O<sub>2</sub> shows better electrical conductivity and smaller charge transfer resistance, beneficial for lowering the overpotential (1.29 V) and enhancing the cycling stability of LOB (157 cycles with a limited capacity of 500 mA h g<sup>−1</sup> at 200 mA g<sup>−1</sup>).

A nitrogen dopant with an analogous atomic size to O and lower ionization energy could induce the formation of V<sub>o</sub> because of charge balancing. Zhang *et al.*<sup>70</sup> synthesized N-doped LaNiO<sub>3</sub> (LNO) with an increased amount of V<sub>o</sub> and Ni<sup>3+</sup>. Ni<sup>3+</sup> with its optimized e<sub>g</sub>-filling orbital (t<sub>2g</sub><sup>6</sup>e<sub>g</sub><sup>1</sup>) is more favorable toward ORR/OER catalytic activity. Furthermore, the generated V<sub>o</sub> enhanced the formation and further decomposition of Li<sub>2</sub>O<sub>2</sub> and hampered side reactions between the cathode and electrolyte (Fig. 6(j)). As a result, the LOB using the LNO cathode reached a high discharge capacity of up to 5910 mA h g<sub>cathode</sub><sup>−1</sup> at 50 mA g<sub>cathode</sub><sup>−1</sup>. Though anion dopants in the O-site have been investigated in semiconductors to adjust the bandgap energy, few studies of anion-doped perovskites as catalysts for LOBs have been reported.

### 4.3 Oxygen vacancy

The role of oxygen defects in perovskites cannot be neglected because they can tune the electronic structure, surface chemistry and crystalline nanostructures, thereby modifying the physicochemical properties of catalysts.<sup>111</sup>

The creation of V<sub>o</sub> modulates the interaction between the B-site TM and oxygen molecules. The e<sub>g</sub>-filling of the B-site cation is a decisive factor in determining oxygen adsorption/desorption energy. A lower e<sub>g</sub>-filling results in strong B–O<sub>2</sub> bonds, and a higher e<sub>g</sub>-filling contributes to weak bonding.<sup>45</sup> As well as the cation doping discussed above, annealing materials under a reducing atmosphere is another viable approach to create V<sub>o</sub> in perovskites. For example, V<sub>o</sub> was introduced to CaMnO<sub>3</sub> through thermal treatment under mixed H<sub>2</sub>/Ar gas at 300 °C. The presence of V<sub>o</sub> in CaMnO<sub>3</sub> created mixed-valence Mn<sup>3+</sup>/Mn<sup>4+</sup> states, modifying the electronic structure of CaMnO<sub>3</sub>.<sup>45</sup> The mixed Mn<sup>4+</sup> (t<sub>2g</sub><sup>3</sup>e<sub>g</sub><sup>0</sup>) and Mn<sup>3+</sup> (t<sub>2g</sub><sup>3</sup>e<sub>g</sub><sup>1</sup>) exhibited an intermediate e<sub>g</sub> occupation,



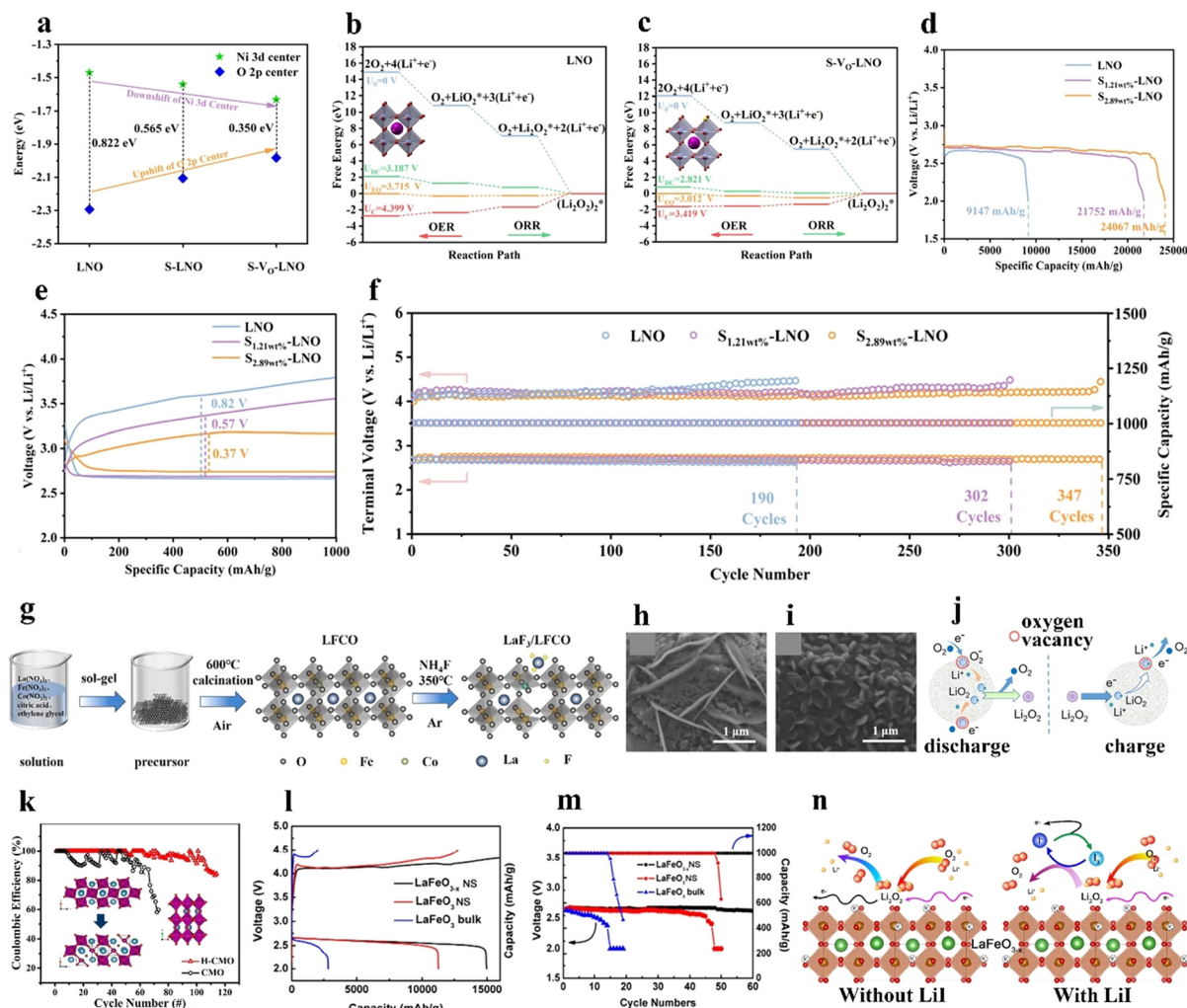


**Fig. 6** The impact of B-site substitution and oxygen vacancies on perovskites. (a) Illustration of Ni 3d and O 2p band centers S-V<sub>O</sub>-LNO and control samples. Free energy diagram of the ORR on (b) LNO and (c) S-V<sub>O</sub>-LNO. (d) Discharge curves at 100 mA g<sup>-1</sup>, (e) discharge/charge curves with a confined capacity of 1000 mA h g<sup>-1</sup> at 100 mA g<sup>-1</sup>. (f) Cycling stability of the LOBs with LNO and S-V<sub>O</sub>-LNO cathodes. (a)–(f) Reproduced with permission.<sup>68</sup> Copyright 2022, Elsevier. (g) Illustration of the synthesis process of LaF<sub>3</sub>/LFCO. SEM images of (h) LFCO and (i) LaF<sub>3</sub>/LFCO cathodes after the first discharge. (g)–(i) Reproduced with permission.<sup>69</sup> Copyright 2022, Elsevier. (j) Formation and decomposition processes of Li<sub>2</sub>O<sub>2</sub> on N-doped LNO during the discharge/charge process. Reproduced with permission.<sup>70</sup> Copyright 2018, American Chemical Society. (k) Coulombic efficiency of H-CMO and CMO. Insets: Their crystal structures. Reproduced with permission.<sup>45</sup> Copyright 2020, American Chemical Society. (l) The initial capacity at 100 mA g<sup>-1</sup> and (m) cycling stability of LaFeO<sub>3</sub> and LaFeO<sub>3-x</sub>. (n) ORR and OER mechanisms on the LaFeO<sub>3-x</sub> surface with/without LiI. (k)–(n) Reproduced with permission.<sup>76</sup> Copyright 2020, Elsevier.

facilitating the formation of superoxide and Li<sub>2</sub>O<sub>2</sub> and resulting in better ORR activity (a smaller Tafel slope of  $-0.756 \text{ V dec}^{-1}$ ). Multiple valences of the B-site cation and unique structural arrangements, along with the good ionic conductivity of perovskite oxides, collectively promote the  $B^{(n+1)+}/B^{n+}$  redox reaction. Accordingly, the LOB using defective CaMnO<sub>3</sub> (H-CMO) provided an improved cycling capability of 114 cycles with a limited capacity of 500 mA h g<sup>-1</sup> at 500 mA g<sup>-1</sup> (Fig. 6(k)). The LOB using H-CMO achieved a higher capacity of around 3600 mA h g<sup>-1</sup> at 250 mA g<sup>-1</sup>, outperforming the cell using CMO (2750 mA h g<sup>-1</sup>).

The presence of V<sub>O</sub> in perovskites optimizes the surface adsorption energy, provides a large body of active sites and promotes Li<sup>+</sup> or e<sup>-</sup> conductivity. Gao *et al.*<sup>76</sup> produced V<sub>O</sub> in

LaFeO<sub>3-x</sub> by calcination of the pristine LaFeO<sub>3</sub> under Ar gas, which distorted the FeO<sub>6</sub> octahedra and changed the valence state of Fe. Theoretical calculation results suggested that O<sub>2</sub> molecules tended to adsorb on the surface-defective sample more than on LaFeO<sub>3</sub>. The existence of Fe with different valence states can increase ionic and electronic conductivity. Accordingly, the LOB with oxygen-defective LaFeO<sub>3-σ</sub> showed a higher initial capacity, better rate capacity, and longer cycle life than that with LaFeO<sub>3</sub> (Fig. 6(l) and (m)). Moreover, an LiI redox mediator was used to further reduce the overpotential due to the I<sub>3</sub><sup>-</sup> to I<sup>-</sup> redox reaction (Fig. 6(n)). However, the lack of accurate control of the V<sub>O</sub> content continues to hamper efforts to quantitatively investigate the structure–activity relationship between V<sub>O</sub> and catalytic activity.



#### 4.4 Perovskite-based composite catalysts

Combining perovskite oxides with conductive substances such as carbon, MOFs, MXene, and metal compounds is a feasible way to enhance their electrochemical activity and overcome their intrinsic low conductivity. The intimate interfacial interplay between dual materials gives rise to unique electronic structures and improved structural stability.

**Perovskite/carbon composites.** Porous carbon materials such as 3D graphene with favorable electrical conductivity, high surface area, and controllable porosity have been used as suitable substrates to load with perovskite oxides, as they not only maximize the utilization of active sites but also facilitate the infiltration of electrolyte.<sup>26,31,74,76,77,94,112,113</sup> A dip-coating method was used to prepare carbon/perovskite composites, in which the carbon substrate is immersed in a precursor solution and surfactant, followed by the hydrolysis and condensation of the precursor.<sup>113</sup> Kim *et al.*<sup>31</sup> hybridized  $\text{Nd}_{1.5}\text{Ba}_{1.5}\text{CoFeMnO}_{9-\delta}$  with N-doped rGO to produce a highly active bifunctional ORR/OER catalyst, which exhibited efficient charge transfer, oxygen-defective structure, and small hybridization strength between Co 3d and O 2p orbitals.

In addition, carbon nanofibers or nanosheets have been adopted as ideal frameworks to load with perovskites as conductive and highly porous free-standing cathodes.<sup>74,113,114</sup> Yang *et al.*<sup>113</sup> prepared sandwich-like graphene/mesoporous  $\text{LaSrMnO}$  nanosheets as free-standing cathodes for LOBs. Mesopores offered a high surface area for loading discharged products and easy access channels for the electrolyte, and served as reservoirs of  $\text{O}_2$  to feed the ORR/OER reactions. Macropores between nanosheets expedited  $\text{Li}^+$  diffusion and  $\text{O}_2$  transport into the inner space of the catalyst. In the composite, the perovskite phase was responsible for decreasing the reaction overpotential, and the graphene foam acted as a conductive medium to promote electron transport, provided sufficient room for the deposition/decomposition of  $\text{Li}_2\text{O}_2$  and prevented the clogging of the discharged resultants. Accordingly, the assembled LOB demonstrated a high specific capacity, rate capability, and long cycling life.

Unfortunately, the electrochemical oxidation of carbon materials under high potentials during the OER process deactivates active sites. Highly active oxygen radicals like  $\text{O}^{2-}$ ,  $\text{LiO}_2$  and  $\text{Li}_2\text{O}_2$  corrode carbon materials, and decompose carbons and organic electrolytes, shortening the cycle life of LOBs.<sup>84</sup> Highly durable frameworks for loading perovskite oxides are thus required.

**Perovskite/MOF composite.** MOFs with well-defined pore structures can act as suitable scaffolds to load perovskite nanoparticles. Their adjustable pore configurations can match the geometry and size of perovskite nanocrystals and guarantee easy accessibility for reagents during synthesis. Qiao<sup>92</sup> confined  $\text{CsPbBr}_3$  nanocrystals into a mesoporous Fe-MOF (4.2 and 5.5 nm) to derive a perovskite/MOF hybrid catalyst ( $\text{CsPbBr}_3@\text{PCN-333(Fe)}$ ) by a sequential deposition method, where perovskite nanocrystals were stabilized from leaching or aggregation due to the confinement effect of the MOF cages.

As shown in Fig. 7(a)–(c), the electrons of  $\text{CsPbBr}_3$  could be completely transferred to the MOF when they were in the cage, while only a fraction of the electrons were transferred to the external interface. No electron transfer happened if  $\text{CsPbBr}_3$  was far away from the MOF. Interestingly, the  $\text{O}_2/\text{Li}_2\text{O}_2$  redox couple resided between the valence band (VB) and conduction band (CB) of  $\text{CsPbBr}_3$  and the MOF (Fig. 7(d)). Photoelectrons and holes in the composite can be excited and then transported to the CB and VB under irradiation, conducive for the use of solar energy. The LOB with a  $\text{CsPbBr}_3@\text{PCN-333(Fe)}$  photocathode demonstrated a high discharge voltage of 3.19 V with a round-trip efficiency of 92.7% and could be stably cycled for above 200 h at  $0.01 \text{ mA cm}^{-2}$  under illumination.

**Perovskite/noble metal composites.** Bifunctional catalysts have been prepared by combining perovskite oxides with novel metal nanoparticles or TM compounds, such as Pd and Ag nanoparticles,  $\text{RuO}_2$ ,  $\text{CoO}$ ,  $\text{Co}_3\text{O}_4$ ,  $\text{Fe}_2\text{O}_3$ , and  $\text{Ni}_3\text{S}_2$ .<sup>25,38,59,73,78–81</sup> Carbon-free catalysts avoid the decomposition of carbon by highly oxidative radicals. Owing to its high catalytic activity and superior electrical conductivity ( $\sim 10^4 \text{ S cm}^{-1}$ ),  $\text{RuO}_2$  has been combined with perovskites to enhance electron-transfer kinetics at the interface between the cathode and oxygen intermediates.<sup>73,115,116</sup> The LiOH reaction product is derived from the reaction between  $\text{Li}_2\text{O}_2$  and  $\text{H}_2\text{O}$ , and  $\text{Li}_2\text{CO}_3$  comes from electrolyte decomposition and the reaction product of carbon and  $\text{Li}_2\text{O}_2$ .<sup>73</sup> Therefore, designing electrocatalysts that can decompose both LiOH and  $\text{Li}_2\text{CO}_3$  is an effective way to boost the performance of LOBs. Sun *et al.*<sup>73</sup> used a wet impregnation method to grow  $\text{RuO}_2$  nanoparticles on a 1D porous  $\text{La}_{0.6}\text{Sr}_{0.4}\text{Co}_{0.8}\text{Mn}_{0.2}\text{O}_3$  nanofiber (LSCM NF). Owing to their good electrical conductivity and superior OER/ORR catalytic performance,  $\text{RuO}_2$  was capable of decomposing LiOH and  $\text{Li}_2\text{O}_2$ , and the LSCM NFs could decompose the reaction side-product of  $\text{Li}_2\text{CO}_3$ . The composite electrode had a large initial capacity of  $12\,742 \text{ mA h g}^{-1}$  at  $50 \text{ mA g}^{-1}$ , a low voltage range of 2.6–4.3 V, and a stable cycle life ( $\geq 100$  cycles with a limited capacity of  $500 \text{ mA h g}^{-1}$  at  $50 \text{ mA g}^{-1}$ ), as shown in Fig. 7(e).

Interestingly, water vapor as an additive was introduced to oxygen gas in the solid-state LOB, which transformed the discharge product from growth-limited  $\text{Li}_2\text{O}_2$  to easily formed LiOH, and improved the specific capacity of the LOB.<sup>38,117</sup> Kim *et al.*<sup>38</sup> hybridized electron conducting  $\text{RuO}_2$  and  $\text{La}_2\text{LiRuO}_{6-\delta}$  as a highly active electrocatalyst for a LiOH-related reaction in a solid-state LOB to increase capacity and cycle life (665 cycles with a limited capacity of  $200 \text{ mA h g}_{\text{cathode}}^{-1}$  at  $100 \text{ mA g}_{\text{cathode}}^{-1}$ ) (Fig. 7(f)). Humidity increased the discharge voltage of the LOB to 3.4 V, surpassing the cell operated under dry oxygen (2.96 V) (Fig. 7(g) and (h)). LiOH was capable of absorbing water vapor and became hydrated LiOH as a  $\text{Li}^+$ -ion conductor, boosting the reaction kinetics.

Furthermore, due to its cheap price, good conductivity, and catalytic activity, metallic Ag has also been combined with perovskites as a cathode for LOBs.<sup>87,118</sup> Zou *et al.*<sup>118</sup> took advantage of the heterostructural interface between the conductive Ag nanoparticles and a  $\text{PrBa}_{0.5}\text{Sr}_{0.5}\text{Co}_2\text{O}_{5+\delta}$  (PBSC)





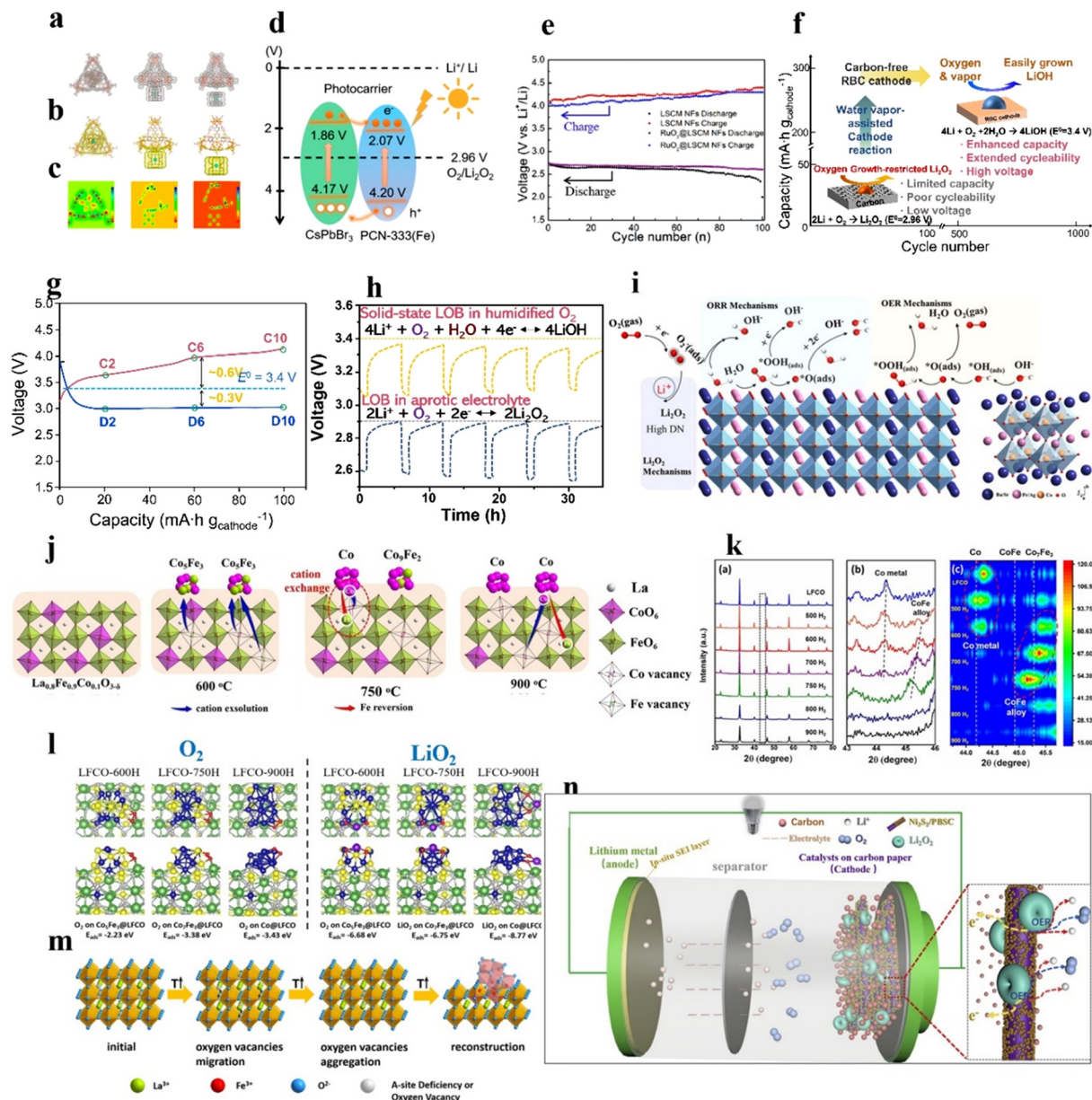


**Fig. 7** Perovskite-based composite catalysts. (a) Charge density of CsPbBr<sub>3</sub> inside the cage, outside the cage, and isolated. (b) Corresponding charge density difference. (c) Corresponding 2D deformation charge density. (d) Demonstration of the VB and CB energy levels and the redistribution of photocarriers between PCN-333(Fe) and CsPbBr<sub>3</sub> under light. (a)–(d) Reproduced with permission.<sup>92</sup> Copyright 2021, American Chemical Society. (e) Discharge/charge terminal voltages of LOBs with RuO<sub>2</sub>@LSCM NF and LSCM NF cathodes. Reproduced with permission.<sup>73</sup> Copyright 2021, American Chemical Society. (f) Schematic illustration of a solid-state LOB. (g) Discharge–charge curves of LOBs in humidified O<sub>2</sub>. (h) Galvanostatic intermittent titration technique (GITT) results of the LOB tested in liquid electrolyte without water vapor. (i) Schematic illustration of the ORR/OER at the Ag/PBSC heterostructure surface. Reproduced with permission.<sup>118</sup> Copyright 2022, Wiley-VCH. (j) Dual-exsolution of LFCO controlled by temperature. (k) XRD patterns, enlarged XRD pattern at 43–46°, and depth view of the XRD pattern at 43.4–45.8° of LFCO. (l) Binding energy of O<sub>2</sub> and LiO<sub>2</sub> on LFCO obtained at different temperatures. (j)–(l) Reproduced with permission.<sup>81</sup> Copyright 2022, Wiley-VCH. (m) Schematic illustration of the preparation of the α-Fe<sub>2</sub>O<sub>3</sub>/LaFeO<sub>3-x</sub> composite. Reproduced with permission.<sup>90</sup> Copyright 2018, American Chemical Society. (n) Schematic illustration of the LOB employing Ni<sub>3</sub>S<sub>2</sub>/PBSC cathodes, and schematic of the charging process. Reproduced with permission.<sup>78</sup> Copyright 2019, Elsevier.

perovskite, and demonstrated that Ag could nucleate Li<sub>2</sub>O<sub>2</sub> with a low overpotential (Fig. 7(i)).

**Perovskite/TM composites.** The crystallinity and morphology of Li<sub>2</sub>O<sub>2</sub> impacts the electrochemical performance of LOBs. Large-sized Li<sub>2</sub>O<sub>2</sub> generally results in a high specific capacity and durable cycling longevity, while a film-like amorphous

discharge product contributes to fast ion and electron transport, exhibiting an easier decomposition process during charging.<sup>24</sup> The metal component and perovskite can synergistically optimize the binding strength with O<sub>2</sub> and LiO<sub>2</sub>, which modulates the discharge reaction pathways. Cong *et al.*<sup>81</sup> prepared a CoFe alloy and Co-metal-decorated La<sub>0.8</sub>Fe<sub>0.9</sub>Co<sub>0.1</sub>O<sub>3-δ</sub>



(LFCO) catalyst by annealing the pristine perovskite under 5% H<sub>2</sub>/Ar atmosphere. With the increased annealing temperature, nanoparticles indexed to the CoFe alloy and Co metal gradually appeared on the surface of the perovskites, as indicated by X-ray diffraction (XRD) results (Fig. 7(j) and (k)). At 600 °C, Co and Fe species exsolved from the parent perovskite to generate an alloy at the surface to form LFCO-600H, while the Fe component in the alloy started to exchange with Co at 750 °C. At 900 °C, the increased Co species finally became a metallic state. DFT calculation results (Fig. 7(l)) indicated that due to the weak adsorption between the CoFe alloy, O<sub>2</sub> and LiO<sub>2</sub>, lithium superoxide was generated at the LFCO-600H surface by a one-electron reduction step and diffused to the electrolyte. It transformed to Li<sub>2</sub>O<sub>2</sub> and O<sub>2</sub> via a disproportionation reaction, generating ring-like Li<sub>2</sub>O<sub>2</sub>. However, the strong binding strength of Co metal in LFCO-900H with O<sub>2</sub>/LiO<sub>2</sub> led to the formation of thin-film-like Li<sub>2</sub>O<sub>2</sub>. Due to the interaction between the CoFe alloy/Co metal and the parent perovskite, as well as a high degree of structural distortion, LFCO-750H demonstrated moderate binding strength. Accordingly, the LOB using the LFCO-750 cathode exhibited a high discharge capacity of 6549.7 mA h g<sup>-1</sup> at 100 mA g<sup>-1</sup> and negligible capacity fading after 215 cycles compared to LFCO-600 and LFCO-900, the samples annealed at 600 °C and 900 °C.

The segregation of TM oxides in A-site defective perovskites can promote LOB performance. For example, the formation of V<sub>o</sub> during the thermal treatment of La<sub>0.85</sub>FeO<sub>3-δ</sub> at 900 °C resulted in the segregation of α-Fe<sub>2</sub>O<sub>3</sub> (Fig. 7(m)).<sup>90</sup> In the composite, the interaction between LaFeO<sub>3-x</sub> and α-Fe<sub>2</sub>O<sub>3</sub> led to structural distortion, exposing ample active sites for the OER/ORR. The LOB with the composite catalyst exhibited a longer cycle life (108 cycles) than that with α-Fe<sub>2</sub>O<sub>3</sub> (21 cycles) and La<sub>0.85</sub>FeO<sub>3-δ</sub> (51 cycles) catalysts. In another example, Ni nanoparticles were exsolved on the La<sub>0.9</sub>Mn<sub>0.6</sub>Ni<sub>0.4</sub>O<sub>3-δ</sub> nanofiber surface during thermal treatment under a H<sub>2</sub>/Ar atmosphere.<sup>88</sup> The interaction between metal nanoparticles and perovskite and the formation of V<sub>o</sub> synergistically increased the number of active sites, and improved electrical conductivity and O<sub>2</sub> adsorption.

Ni, Co, and Fe-based compounds with favorable catalytic activity have been combined with perovskites to prepare hybrid catalysts with the collective superiorities of dual-functional materials. Zhang *et al.*<sup>78</sup> used an atomic-layer-deposition approach to deposit a layer of Ni<sub>3</sub>S<sub>2</sub> (10 nm) on 1D PrBa<sub>0.5</sub>Sr<sub>0.5</sub>Co<sub>2</sub>O<sub>5+δ</sub> (PBSC) nanofibers as an integrated catalyst. The Li<sub>2</sub>O<sub>2</sub> discharge product could be effectively decomposed to Li<sup>+</sup> and O<sub>2</sub> by virtue of the high OER activity of the PBSC and Ni<sub>3</sub>S<sub>2</sub>. The peroxide combined with V<sub>o</sub> in the PBSC and then oxidized to oxygen, and the nanosized Ni<sub>3</sub>S<sub>2</sub> and unique 1D porous PBSC could rapidly transfer electrons from active sites to the current collector. The assembled LOB (Fig. 7(n)) showed a low overpotential of 0.68 V at 1000 mA h g<sup>-1</sup>, large capacity (12 874 mA h g<sup>-1</sup> at 100 mA g<sup>-1</sup>), and long cycle life (>120 cycles with a limited capacity of 1000 mA h g<sup>-1</sup> at 100 mA g<sup>-1</sup>). Another example shows that FeOOH clusters on the LaNiO<sub>3</sub> surface enhanced OH<sup>-</sup> adsorption and weakened

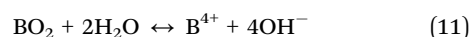
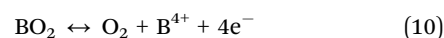
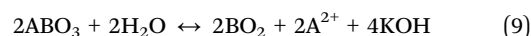
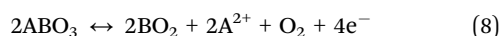
the Ni–O bond in an alkaline electrolyte, which optimized the OH<sup>-</sup> filling barrier to boost the lattice O-involved OER and decreased the reaction barrier of the LOM.<sup>59</sup> Co<sub>3</sub>O<sub>4</sub> nanoparticles on LaCo<sub>0.6</sub>Ni<sub>0.4</sub>O<sub>3</sub> facilitated O<sub>2</sub> adsorption on the catalyst surface and O<sub>2</sub>/Li<sub>2</sub>O<sub>2</sub> conversion.<sup>119</sup> In addition to the above-mentioned materials, Ti<sub>3</sub>C<sub>2</sub>T<sub>x</sub> nanosheets with low Li ionic diffusion barriers (<0.07 eV) have been used as substrates to load La<sub>0.5</sub>Sr<sub>0.5</sub>CoO<sub>3-δ</sub> perovskite as a catalyst for LOBs.<sup>27</sup> The derived LOB could be operated over 80 cycles at 500 mA g<sup>-1</sup> with a restriction of 1000 mA h g<sup>-1</sup>, superior performance to that of La<sub>0.5</sub>Sr<sub>0.5</sub>CoO<sub>3-δ</sub> (15 cycles) and Ti<sub>3</sub>C<sub>2</sub>T<sub>x</sub> (9 cycles).

## 5. Conclusion

Perovskite oxides have been studied as promising ORR/OER electrocatalysts due to their favorable catalytic activity, tunable compositions and nanostructures. This mini-review analyzes the recent advances in perovskite oxide electrocatalysts for LOBs, and highlights the synthetic techniques, fundamental catalytic mechanisms, and various strategies for the enhancement of catalytic performance. There is ample space to advance this technology by exploring the ORR/OER mechanisms, porous structure development, composition regulation, defect engineering, and composite synthesis for perovskite oxides in nonaqueous LOBs. Below is a summary of the existing challenges in the use of perovskite oxides as catalysts.

(i) Notwithstanding massive endeavors to study the catalytic mechanisms of perovskite oxides for the ORR/OER in aqueous electrolytes, the investigation of fundamental catalytic mechanisms in the nonaqueous electrolyte scenario is still in its infancy. The relationship between the composition, crystal structure, and catalytic performance needs to be clarified and deeply investigated, as this knowledge is critical for guiding the design of highly active catalysts for LOBs.

It should be noted that in aqueous alkaline electrolytes, *in situ* surface reconstruction or amorphization of perovskites could occur by anodic polarization during the OER, which has been proved to be beneficial for enhancing the OER performance.<sup>120–122</sup> A-site cations have high solubility in alkaline electrolytes, and BO<sub>2</sub> metal oxides also suffer from chemical dissolution during the lattice-involved OER process. The dissolved B-site cations either release to the bulk electrolyte or react with OH<sup>-</sup> ions and then deposit on the material surface to form an oxyhydroxide phase.<sup>123</sup> The processes can be described in eqn (8)–(11):



Of particular note, the surface reconstruction of perovskites in nonaqueous electrolytes has rarely been studied. It is speculated that it could occur when the surface lattice oxygen



participates in the catalytic process. More explicitly, the active lattice oxygen of perovskites can assist in adsorbing  $\text{Li}^+$  ions from the aprotic electrolyte due to its shallower O 2p band adjacent to the Fermi level to donate electrons.<sup>61</sup> After that, the generated electrophilic oxyl groups on the surface serve as initial growth species to react with nucleophilic moieties like  $\text{LiO}_2$ , triggering the formation of the discharge product.<sup>17,61</sup> Even though the surface lattice oxygen as catalytic sites has been proved to improve the ORR/OER kinetics, it may give rise to the generation of surface oxygen defects. Oxygen defects will be compensated by generating cationic vacancies, leading to the dissolution of surface cations and eventually resulting in the instability of the catalyst surface.<sup>61,124</sup> As a result, the surface composition and nanostructure of perovskites are altered due to the formation of oxygen defects and the dissolution of surface cations. In this regard, the change in the surface electronic structure, crystallinity, valence state, and coordination environment of cations, and morphology of perovskite oxides upon cycling can be investigated by *in situ* or *ex situ* characterizations such as *in situ* TEM, Raman, X-ray absorption spectroscopy, *etc.* These techniques help to understand how these changes influence the catalytic activity and durability of cathodes for LOB. The combination of results from advanced characterization, experiments, and theoretical calculations is required for a comprehensive understanding of the underlying mechanisms of the reaction occurring at specific active sites under operando status.

(ii) Myriad cations or anions can be accommodated at the A-, B-, and O-sites of perovskites, ensuring the versatile adjustment of their properties for optimized catalytic performance. Screening and synthesis of ideal perovskite oxide catalysts are challenging and tedious processes due to the multitude of choices of elements. Therefore, artificial intelligence such as machine learning and high-throughput calculations can be used to gain unique insights and to screen highly active catalysts based on data sets. This will enable researchers to design materials with optimized compositions and ideal experimental parameters.<sup>29,125,126</sup>

(iii) High specific surface areas and controllable porosities are required to provide ample catalytically active spots and allow easy transport of reactants. It is known that the large-area triple boundaries, where oxygen, electrolyte, and oxygen cathodes exist, play crucial roles in effectively transporting mass and accommodating the discharged products. However, perovskite oxide catalysts prepared by the current synthetic methods (*e.g.*, sol-gel and solid-state reaction) show a small SSA ( $<300 \text{ m}^2 \text{ g}^{-1}$ ), uncontrollable pore structures, and irregular morphology in some cases, impeding mass transport. Novel 3D-printed ordered perovskite,<sup>127</sup> self-assembled anti-perovskites,<sup>128</sup> and 3D structured perovskitoids<sup>39</sup> with large SSAs, controllable morphologies and tailorable porous architectures may overcome these challenges, and are promising cathode candidates for LOBs.

(iv) It is imperative to pay attention to the activity-stability tradeoff of perovskites. Long cycling stability of energy-storage devices is a prerequisite for real-world applications, while LOBs

with perovskite cathodes can be operated for only several hundred cycles ( $<200$  cycles in many cases), which is unfavorable for practical applications. The poor cycling stability of LOB batteries with perovskite cathodes can be attributed to the following reasons. First, the insoluble  $\text{Li}_2\text{O}_2$  product covered on the perovskite surface blocks oxygen diffusion pathways, leading to severe volume expansion of the air cathode, and inducing side reactions at the cathode.<sup>20</sup> Due to limited active sites at the  $\text{Li}_2\text{O}_2$ /catalyst interface, voltage polarization could occur and the reaction kinetics for the ORR/OER become sluggish.<sup>20</sup> Second, metal elements in perovskites facilitate the generation of metal-O bonds in an  $\text{O}_2$ -rich environment, which may gradually degrade the material structure. Third, some perovskites can be partially decomposed in aprotic solvents. For example, due to the reaction between positive  $\text{Pb}^{2+}$  ions and polar aprotic solvents, the  $\text{PbI}_6$  octahedral framework collapsed in a trihalide perovskite.<sup>129</sup> Moreover, the improved catalytic activity of surface lattice oxygen of perovskites is at the expense of surface stability, where surface cations will be dissolved in the electrolyte, and bulk cation ions migrate to the surface area, resulting in instability of perovskite structures. To circumvent these obstacles, a porous structure of the cathode is highly required to increase oxygen diffusion paths and the number of nucleation sites for the discharged product, effectively decreasing the overpotential during charging/discharging processes of LOBs. Furthermore, soluble redox mediators could be introduced to the electrolyte to tune the formation and decomposition pathways of  $\text{Li}_2\text{O}_2$  for further decreasing the overpotential of the ORR and OER. On top of that, nanostructured perovskite oxides (nanocrystals or quantum dots) can be combined with large-surface-area materials, such as graphene, porous carbon, MOFs, and covalent organic frameworks to harness the collaborative benefits of multiple active components. Meanwhile, a high loading of perovskite oxide on the substrates is required to achieve high catalytic performance.

## Conflicts of interest

The authors declare no competing interests.

## Acknowledgements

This research was supported by Creative Materials Discovery Program through the National Research Foundation of Korea (NRF) funded by Ministry of Science and ICT (NRF-2020M3D1A1110522 and NRF-2022R1A2B5B03001781).

## References

- 1 J. L. Holechek, H. M. E. Geli, M. N. Sawalhah and R. Valdez, *Sustainability*, 2022, **14**, 4792.
- 2 R. Zhang, H. Zhou, P. Sun, Q. Ma, M. Lu, H. Su, W. Yang and Q. Xu, *Battery Energy*, 2022, **1**, 20220023.





- 3 C. Y. J. Lim and Z. W. Seh, *Battery Energy*, 2022, **1**, 20220008.
- 4 Y. Guo, Y. Zhang and H. Lu, *Battery Energy*, 2022, **1**, 20210014.
- 5 C. Shu, J. Wang, J. Long, H. K. Liu and S. X. Dou, *Adv. Mater.*, 2019, **31**, 1804587.
- 6 M. D. Radin and D. J. Siegel, *Energy Environ. Sci.*, 2013, **6**, 2370–2379.
- 7 T. Liu, J. P. Vivek, E. W. Zhao, J. Lei, N. Garcia-Araez and C. P. Grey, *Chem. Rev.*, 2020, **120**, 6558–6625.
- 8 W. J. Kwak, R. Sharma, D. Sharon, C. Xia, H. Kim, L. R. Johnson, P. G. Bruce, L. F. Nazar, Y. K. Sun, A. A. Frimer, M. Noked, S. A. Freunberger and D. Aurbach, *Chem. Rev.*, 2020, **120**, 6626–6683.
- 9 K. Yoo, S. Banerjee, J. Kim and P. Dutta, *Energies*, 2017, **10**, 1748.
- 10 M. Park, C. Liang, T. H. Lee, D. A. Agyeman, J. Yang, V. W. Hei Lau, S. Il Choi, H. W. Jang, K. Cho and Y. M. Kang, *Adv. Energy Mater.*, 2020, **10**, 1903225.
- 11 Y. K. Jo, W. Tamakloe, X. Jin, J. Lim, S. B. Patil, Y. M. Kang and S. J. Hwang, *Appl. Catal., B*, 2019, **254**, 523–530.
- 12 Y. Bae, H. Park, Y. Ko, H. Kim, S. K. Park and K. Kang, *Batteries Supercaps*, 2019, **2**, 311–325.
- 13 T. H. Gu, D. A. Agyeman, S. J. Shin, X. Jin, J. M. Lee, H. Kim, Y. M. Kang and S. J. Hwang, *Angew. Chem., Int. Ed.*, 2018, **130**, 16216–16221.
- 14 K. Song, J. Jung, M. Park, H. Park, H. J. Kim, S. Il Choi, J. Yang, K. Kang, Y. K. Han and Y. M. Kang, *ACS Catal.*, 2018, **8**, 9006–9015.
- 15 D. A. Agyeman, M. Park and Y. M. Kang, *J. Mater. Chem. A*, 2017, **5**, 22234–22241.
- 16 K. Song, E. Cho and Y. M. Kang, *ACS Catal.*, 2015, **5**, 5116–5122.
- 17 Y. Zheng, K. Song, J. Jung, C. Li, Y. U. Heo, M. S. Park, M. Cho, Y. M. Kang and K. Cho, *Chem. Mater.*, 2015, **27**, 3243–3249.
- 18 D. A. Agyeman, K. Song, S. H. Kang, M. R. Jo, E. Cho and Y. M. Kang, *J. Mater. Chem. A*, 2015, **3**, 22557–22563.
- 19 H. Song, R. Choi, J. Jung, G. Kim, K. Song, Y. Il Kim, S. C. Jung, Y. K. Han and Y. M. Kang, *Energy Environ. Sci.*, 2014, **7**, 1362–1368.
- 20 Z. Chang, J. Xu and X. Zhang, *Adv. Energy Mater.*, 2017, **7**, 1700875.
- 21 W. Bai, Z. Zhang, K. Wang and J. Chen, *Battery Energy*, 2022, **1**, 20220019.
- 22 Y. Lai, Y. Jiao, J. Song, K. Zhang, J. Li and Z. Zhang, *Mater. Chem. Front.*, 2018, **2**, 376–384.
- 23 Y. Yang, X. Xue, Y. Qin, X. Wang, M. Yao, Z. Qin and H. Huang, *J. Phys. Chem. C*, 2018, **122**, 12665–12672.
- 24 Y. Liu, J. Cai, J. Zhou, Y. Zang, X. Zheng, Z. Zhu, B. Liu, G. Wang and Y. Qian, *eScience*, 2022, **2**, 389–398.
- 25 J. Wang, X. Cheng, Z. Li, M. Xu, Y. Lu, S. Liu, Y. Zhang and C. Sun, *ACS Appl. Energy Mater.*, 2018, **1**, 5557–5566.
- 26 J. Cheng, Y. Jiang, M. Zhang, L. Zou, Y. Huang, Z. Wang, B. Chi, J. Pu and J. Li, *Phys. Chem. Chem. Phys.*, 2017, **19**, 10227–10230.
- 27 Z. Sun, M. Yuan, L. Lin, H. Yang, C. Nan, G. Sun, H. Li and X. Yang, *ACS Appl. Energy Mater.*, 2019, **2**, 4144–4150.
- 28 W. Xiong, H. Yin, T. Wu and H. Li, *Eur. J. Chem.*, 2022, **29**, e202202872.
- 29 J. Hwang, R. R. Rao, L. Giordano, Y. Katayama, Y. Yu and Y. Shao-Horn, *Science*, 2017, **358**, 751–756.
- 30 Q. Ji, L. Bi, J. Zhang, H. Cao and X. S. Zhao, *Energy Environ. Sci.*, 2020, **13**, 1408–1428.
- 31 N. I. Kim, Y. J. Sa, T. S. Yoo, S. R. Choi, R. A. Afzal, T. Choi, Y. S. Seo, K. S. Lee, J. Y. Hwang, W. S. Choi, S. H. Joo and J. Y. Park, *Sci. Adv.*, 2018, **4**, eaap9360.
- 32 J. Suntivich, K. J. May, H. A. Gasteiger, J. B. Goodenough, Y. Shao-horn, F. Calle-vallejo, A. D. Oscar, M. J. Kolb, M. T. M. Koper, J. Suntivich, K. J. May, H. A. Gasteiger, J. B. Goodenough and Y. Shao-horn, *Science*, 2011, **334**, 1383–1385.
- 33 J. Suntivich, H. A. Gasteiger, N. Yabuuchi, H. Nakanishi, J. B. Goodenough and Y. Shao-Horn, *Nat. Chem.*, 2011, **3**, 546–550.
- 34 M. A. Peña and J. L. G. Fierro, *Chem. Rev.*, 2001, **101**, 1981–2017.
- 35 J. X. Flores-Lasluisa, F. Huerta, D. Cazorla-Amorós and E. Morallón, *Environ. Res.*, 2022, **214**, 113731.
- 36 K.-L. Wang, Y.-G. Yang, Y.-H. Lou, M. Li, F. Igbari, J.-J. Cao, J. Chen, W.-F. Yang, C. Dong, L. Li, R.-Z. Tai and Z.-K. Wang, *eScience*, 2021, **1**, 53–59.
- 37 X. Li, W. Ma, D. Liang, W. Cai, S. Zhao and Z. Zang, *eScience*, 2022, **2**, 646–654.
- 38 M. Kim, H. Lee, H. J. Kwon, S. Bak, C. Jaye, D. A. Fischer, G. Yoon, J. O. Park, D. Seo, S. B. Ma and D. Im, *Sci. Adv.*, 2022, **2**, eabm8584.
- 39 Y. Miao, X. Wang, H. Zhang, T. Zhang, N. Wei, X. Liu, Y. Chen, J. Chen and Y. Zhao, *eScience*, 2021, **1**, 91–97.
- 40 S. Zhou, X. Miao, X. Zhao, C. Ma, Y. Qiu, Z. Hu, J. Zhao, L. Shi and J. Zeng, *Nat. Commun.*, 2016, **7**, 11510.
- 41 B. Zhao, L. Zhang, D. Zhen, S. Yoo, Y. Ding, D. Chen, Y. Chen, Q. Zhang, B. Doyle, X. Xiong and M. Liu, *Nat. Commun.*, 2017, **8**, 14586.
- 42 M. Sung, G. Lee and D. Kim, *InfoMat*, 2021, **3**, 1295–1310.
- 43 D. Du, R. Zheng, X. Chen, W. Xiang, C. Zhao, B. Zhou, R. Li, H. Xu and C. Shu, *ACS Appl. Mater. Interfaces*, 2021, **13**, 33133–33146.
- 44 X. Liu, H. Gong, T. Wang, H. Guo, L. Song, W. Xia, B. Gao, Z. Jiang, L. Feng and J. He, *Chem. – Asian J.*, 2018, **13**, 528–535.
- 45 G. S. Hegde, A. Ghosh, R. Badam, N. Matsumi and R. Sundara, *ACS Appl. Energy Mater.*, 2020, **3**, 1338–1348.
- 46 H. Wang, M. Zhou, P. Choudhury and H. Luo, *Appl. Mater. Today*, 2019, **16**, 56–71.
- 47 K. Wang, C. Han, Z. Shao, J. Qiu, S. Wang and S. Liu, *Adv. Funct. Mater.*, 2021, **31**, 2102089.
- 48 M. Zhang, G. Jeerh, P. Zou, R. Lan, M. Wang, H. Wang and S. Tao, *Mater. Today*, 2021, **49**, 351–377.
- 49 D. Aurbach, B. D. McCloskey, L. F. Nazar and P. G. Bruce, *Nat. Energy*, 2016, **1**, 16128.
- 50 R. Jacobs, J. Hwang, Y. Shao-Horn and D. Morgan, *Chem. Mater.*, 2019, **31**, 785–797.



- 51 H. Lee, O. Gwon, K. Choi, L. Zhang, J. Zhou, J. Park, J. W. Yoo, J. Q. Wang, J. H. Lee and G. Kim, *ACS Catal.*, 2020, **10**, 4664–4670.
- 52 X. Wu, W. Yu, K. Wen, H. Wang, X. Wang, C. W. Nan and L. Li, *J. Energy Chem.*, 2021, **60**, 135–149.
- 53 A. Khetan, A. Luntz and V. Viswanathan, *J. Phys. Chem. Lett.*, 2015, **6**, 1254–1259.
- 54 Y. Zhou, Y. Zhao, Z. Liu, Z. Peng, L. Wang and W. Chen, *J. Energy Chem.*, 2021, **55**, 55–61.
- 55 X. Gao, Y. Chen, L. Johnson and P. G. Bruce, *Nat. Mater.*, 2016, **15**, 882–888.
- 56 Q. Li, J. Wu, T. Wu, H. Jin, N. Zhang, J. Li, W. Liang, M. Liu, L. Huang and J. Zhou, *Adv. Funct. Mater.*, 2021, **31**, 2102002.
- 57 Y. Zhu, W. Zhou, Z. G. Chen, Y. Chen, C. Su, M. O. Tadé and Z. Shao, *Angew. Chem., Int. Ed.*, 2015, **54**, 3897–3901.
- 58 S. Yagi, I. Yamada, H. Tsukasaki, A. Seno, M. Murakami, H. Fujii, H. Chen, N. Umezawa, H. Abe, N. Nishiyama and S. Mori, *Nat. Commun.*, 2015, **6**, 8249.
- 59 J.-W. Zhao, C.-F. Li, Z.-X. Shi, J.-L. Guan and G.-R. Li, *Research*, 2020, **2020**, 1–15.
- 60 A. Grimaud, O. Diaz-Morales, B. Han, W. T. Hong, Y. L. Lee, L. Giordano, K. A. Stoerzinger, M. T. M. Koper and Y. Shao-Horn, *Nat. Chem.*, 2017, **9**, 457–465.
- 61 D. A. Agyeman, Y. Zheng, T. H. Lee, M. Park, W. Tamakloe, G. H. Lee, H. W. Jang, K. Cho and Y. M. Kang, *ACS Catal.*, 2021, **11**, 424–434.
- 62 J. S. Yoo, X. Rong, Y. Liu and A. M. Kolpak, *ACS Catal.*, 2018, **8**, 4628–4636.
- 63 Y. Pan, X. Xu, Y. Zhong, L. Ge, Y. Chen, J. P. M. Veder, D. Guan, R. O'Hayre, M. Li, G. Wang, H. Wang, W. Zhou and Z. Shao, *Nat. Commun.*, 2020, **11**, 2002.
- 64 C. Yang and A. Grimaud, *Catalysts*, 2017, **7**, 149.
- 65 X. Rong, J. Parolin and A. M. Kolpak, *ACS Catal.*, 2016, **6**, 1153–1158.
- 66 Y. Zhou, Q. Gu, Y. Li, L. Tao, H. Tan, K. Yin, J. Zhou and S. Guo, *Nano Lett.*, 2021, **21**, 4861–4867.
- 67 D. Du, R. Zheng, M. He, C. Zhao, B. Zhou, R. Li, H. Xu, X. Wen, T. Zeng and C. Shu, *Energy Storage Mater.*, 2021, **43**, 293–304.
- 68 R. Li, J. Long, M. Li, D. Du, L. Ren, B. Zhou, C. Zhao, H. Xu, X. Wen, T. Zeng and C. Shu, *Mater. Today Chem.*, 2022, **24**, 100889.
- 69 H. Hou, Y. Cong, Q. Zhu, Z. Geng, X. Wang, Z. Shao, X. Wu, K. Huang and S. Feng, *Chem. Eng. J.*, 2022, **448**, 137684.
- 70 J. Zhang, C. Zhang, W. Li, Q. Guo, H. Gao, Y. You, Y. Li, Z. Cui, K. C. Jiang, H. Long, D. Zhang and S. Xin, *ACS Appl. Mater. Interfaces*, 2018, **10**, 5543–5550.
- 71 H. Gong, T. Wang, H. Guo, X. Fan, X. Liu, L. Song, W. Xia, B. Gao, X. Huang and J. He, *J. Mater. Chem. A*, 2018, **6**, 16943–16949.
- 72 Z. Wang, L. Zou, S. Guo, M. Sun, Y. Chen, B. Chi, J. Pu and J. Li, *J. Power Sources*, 2020, **468**, 228362.
- 73 X. Zhang, Y. Gong, S. Li and C. Sun, *ACS Catal.*, 2017, **7**, 7737–7747.
- 74 T. V. Pham, H. P. Guo, W. Bin Luo, S. L. Chou, J. Z. Wang and H. K. Liu, *J. Mater. Chem. A*, 2017, **5**, 5283–5289.
- 75 X. Li, Z. Qian, G. Han, B. Sun, P. Zuo, C. Du, Y. Ma, H. Huo, S. Lou and G. Yin, *ACS Appl. Mater. Interfaces*, 2020, **12**, 10452–10460.
- 76 R. Gao, Q. Chen, W. Zhang, D. Zhou, D. Ning, G. Schumacher, D. Smirnov, L. Sun and X. Liu, *J. Catal.*, 2020, **384**, 199–207.
- 77 R. S. Kalubarme, G.-E. Park, K.-N. Jung, K.-H. Shin, W.-H. Ryu and C.-J. Park, *J. Electrochem. Soc.*, 2014, **161**, A880–A889.
- 78 Z. Zhang, K. Tan, Y. Gong, H. Wang, R. Wang, L. Zhao and B. He, *J. Power Sources*, 2019, **437**, 226908.
- 79 C. Gong, L. Zhao, S. Li, H. Wang, Y. Gong, R. Wang and B. He, *Electrochim. Acta*, 2018, **281**, 338–347.
- 80 M. Y. Oh, J. H. Kim, Y. W. Lee, K. J. Kim, H. R. Shin, H. Park, K. T. Lee, K. Kang and T. H. Shin, *ACS Appl. Energy Mater.*, 2019, **2**, 8633–8640.
- 81 Y. Cong, Z. Geng, Q. Zhu, H. Hou, X. Wu, X. Wang, K. Huang and S. Feng, *Angew. Chem., Int. Ed.*, 2021, **60**, 23380–23387.
- 82 J. J. Xu, D. Xu, Z. L. Wang, H. G. Wang, L. L. Zhang and X. B. Zhang, *Angew. Chem., Int. Ed.*, 2013, **52**, 3887–3890.
- 83 H. Kim, Y. S. Lim and J. H. Kim, *Chem. Eng. J.*, 2022, **431**, 134278.
- 84 Q. Qiu, Z. Pan, P. Yao, J. Yuan, C. Xia and Y. Zhao, *Chem. Eng. J.*, 2023, **452**, 139608.
- 85 J. J. Xu, Z. L. Wang, D. Xu, F. Z. Meng and X. B. Zhang, *Energy Environ. Sci.*, 2014, **7**, 2213–2219.
- 86 P. Sennu, V. Aravindan, K. S. Nahm and Y. S. Lee, *J. Mater. Chem. A*, 2017, **5**, 18029–18037.
- 87 Z. Wang, X. Peng, S. Guo, M. Sun, J. Cheng, L. Zou, B. Chi and J. Pu, *ACS Appl. Energy Mater.*, 2021, **4**, 9376–9383.
- 88 S. Guo, L. Zou, M. Sun, Z. Wang, S. Han, B. Chi, J. Pu and J. Li, *ACS Appl. Energy Mater.*, 2020, **3**, 10015–10022.
- 89 J. G. Kim, Y. Kim, Y. Noh, S. Lee, Y. Kim and W. B. Kim, *ACS Appl. Mater. Interfaces*, 2018, **10**, 5429–5439.
- 90 Y. Cong, Z. Geng, Y. Sun, L. Yuan, X. Wang, X. Zhang, L. Wang, W. Zhang, K. Huang and S. Feng, *ACS Appl. Mater. Interfaces*, 2018, **10**, 25465–25472.
- 91 J. Jung, K. Song, Y. Bae, S. Il Choi, M. Park, E. Cho, K. Kang and Y. M. Kang, *Nano Energy*, 2015, **18**, 71–80.
- 92 G. Y. Qiao, D. Guan, S. Yuan, H. Rao, X. Chen, J. A. Wang, J. S. Qin, J. J. Xu and J. Yu, *J. Am. Chem. Soc.*, 2021, **143**, 14253–14260.
- 93 J. Kim, H. Kim, S. Shin, H. W. Lee and J. H. Kim, *Electrochim. Acta*, 2022, **412**, 140097.
- 94 Y. Bu, G. Nam, S. Kim, K. Choi, Q. Zhong, J. H. Lee, Y. Qin, J. Cho and G. Kim, *Small*, 2018, **14**, 1802767.
- 95 H. Lin, P. Liu, S. Wang, Z. Zhang, Z. Dai, S. Tan and D. Chen, *J. Power Sources*, 2019, **412**, 701–709.
- 96 J. Zhang, Y. Zhao, X. Zhao, Z. Liu and W. Chen, *Sci. Rep.*, 2014, **4**, 2–7.
- 97 M. Sun, L. Zou, Z. Wang, S. Guo, Y. Chen, B. Chi, J. Pu and J. Li, *Electrochim. Acta*, 2019, **327**, 135017.
- 98 X. Li, T. Zhu, C. Wen, Y. Yang, S. Ma, X. Huang, H. Li and G. Sun, *Electrochim. Acta*, 2019, **317**, 367–374.
- 99 X. Han, Y. Hu, J. Yang, F. Cheng and J. Chen, *Chem. Commun.*, 2014, **50**, 1497–1499.



- 100 Y. Zhu, W. Zhou, J. Yu, Y. Chen, M. Liu and Z. Shao, *Chem. Mater.*, 2016, **28**, 1691–1697.
- 101 X. Xu, Y. Pan, L. Ge, Y. Chen, X. Mao, D. Guan, M. Li, Y. Zhong, Z. Hu, V. K. Peterson, M. Saunders, C. Te Chen, H. Zhang, R. Ran, A. Du, H. Wang, S. P. Jiang, W. Zhou and Z. Shao, *Small*, 2021, **17**, 2101573.
- 102 Y. Bu, O. Gwon, G. Nam, H. Jang, S. Kim, Q. Zhong, J. Cho and G. Kim, *ACS Nano*, 2017, **11**, 11594–11601.
- 103 V. Celorrio, L. Calvillo, G. Granozzi, A. E. Russell and D. J. Fermin, *Top. Catal.*, 2018, **61**, 154–161.
- 104 I. Yamada, H. Fujii, A. Takamatsu, H. Ikeno, K. Wada, H. Tsukasaki, S. Kawaguchi, S. Mori and S. Yagi, *Adv. Mater.*, 2017, **29**, 1603004.
- 105 U. A. Palikundwar, V. B. Sapre, S. V. Moharil and K. R. Priolkar, *J. Phys.: Condens. Matter*, 2009, **21**, 235405.
- 106 J. Cheng, Y. Jiang, M. Zhang, Y. Sun, L. Zou, B. Chi, J. Pu and L. Jian, *ChemCatChem*, 2018, **10**, 1635–1642.
- 107 Z. Du, P. Yang, L. Wang, Y. Lu, J. B. Goodenough, J. Zhang and D. Zhang, *J. Power Sources*, 2014, **265**, 91–96.
- 108 Y. Lv, Z. Li, Y. Yu, J. Yin, K. Song, B. Yang, L. Yuan and X. Hu, *J. Alloys Compd.*, 2019, **801**, 19–26.
- 109 S. Peng, X. Han, L. Li, S. Chou, D. Ji, H. Huang, Y. Du, J. Liu and S. Ramakrishna, *Adv. Energy Mater.*, 2018, **8**, 1800612.
- 110 J. Ran, T. Wang, J. Zhang, Y. Liu, C. Xu, S. Xi and D. Gao, *Chem. Mater.*, 2020, **32**, 3439–3446.
- 111 R. B. Wexler, G. S. Gautam, E. B. Stechel and E. A. Carter, *J. Am. Chem. Soc.*, 2021, **143**, 13212–13227.
- 112 S. Biniyazi, H. Asgharzadeh, I. Ahadzadeh, O. Aydin and M. Farsak, *Dalton Trans.*, 2022, **51**, 18284–18295.
- 113 Y. Yang, W. Yin, S. Wu, X. Yang, W. Xia, Y. Shen, Y. Huang, A. Cao and Q. Yuan, *ACS Nano*, 2016, **10**, 1240–1248.
- 114 L. Zou, S. Guo, Z. Wang, M. Sun, F. Yu, B. Chi and J. Pu, *Electrochim. Acta*, 2021, **381**, 138219.
- 115 Y. Gong, X. Zhang, Z. Li, Z. Wang, C. Sun and L. Chen, *ChemNanoMat*, 2017, **3**, 485–490.
- 116 K. R. Yoon, D. S. Kim, W. H. Ryu, S. H. Song, D. Y. Youn, J. W. Jung, S. Jeon, Y. J. Park and I. D. Kim, *ChemSusChem*, 2016, **9**, 2080–2088.
- 117 Q. Cui, L. Ma, P. Zhang, Y. Cao and J. Wang, *J. Energy Chem.*, 2021, **57**, 401–405.
- 118 L. Zou, Z. Lu, Z. Wang, B. Chi and J. Pu, *J. Am. Ceram. Soc.*, 2022, **105**, 2690–2701.
- 119 M. Sun, S. Guo, Z. Wang, L. Zou, B. Chi, J. Pu and J. Li, *Electrochim. Acta*, 2020, **363**, 137235.
- 120 Y. Fang, Y. Fang, R. Zong, Z. Yu, Y. Tao and J. Shao, *J. Mater. Chem. A*, 2022, **10**, 1369–1379.
- 121 H. Li, Y. Chen, J. Z. Y. Seow, C. Liu, A. C. Fisher, J. W. Ager and Z. J. Xu, *Small Sci.*, 2022, **2**, 2100048.
- 122 B. Bao, Y. Liu, M. Sun, B. Huang, Y. Hu, P. Da, D. Ji, P. Xi and C. H. Yan, *Small*, 2022, **18**, 2201131.
- 123 C. E. Beall, E. Fabbri and T. J. Schmidt, *ACS Catal.*, 2021, **11**, 3094–3114.
- 124 A. Grimaud, A. Demortiere, M. Saubanere, W. Dachraoui, M. Duchamp, M. L. Doublet and J. M. Tarascon, *Nat. Energy*, 2017, **2**, 16189.
- 125 J. A. Esterhuizen, B. R. Goldsmith and S. Linic, *Nat. Catal.*, 2022, **5**, 175–184.
- 126 A. Chen, X. Zhang and Z. Zhou, *InfoMat*, 2020, **2**, 553–576.
- 127 X. Huang, Q. Guo, D. Yang, X. Xiao, X. Liu, Z. Xia, F. Fan, J. Qiu and G. Dong, *Nat. Photonics*, 2020, **14**, 82–88.
- 128 Q. Liang, Y. Zhao, J. De Chen, J. J. Dai, X. Ding, Z. Tong, S. J. Xie, J. Zhang, Z. H. Zhou, J. T. Li, J. F. Li and Y. Zhou, *Chem. Mater.*, 2022, **34**, 5607–5620.
- 129 B. J. Kim, D. H. Kim, S. L. Kwon, S. Y. Park, Z. Li, K. Zhu and H. S. Jung, *Nat. Commun.*, 2016, **7**, 11735.

